

A junctional cAMP compartment regulates rapid Ca^{2+} signaling in atrial myocytes

Sören Brandenburg^{a,b,c,*}, Jan Pawlowitz^a, Vanessa Steckmeister^d, Hariharan Subramanian^e, Dennis Uhlenkamp^a, Marina Scardigli^{f,g}, Mufassra Mushtaq^a, Saskia I. Amlaz^{a,c}, Tobias Kohl^{a,c}, Jörg W. Wegener^{a,c}, Demetrios A. Arvanitis^h, Despina Sanoudou^h, Leonardo Sacconi^{g,i}, Gerd Hasenfuß^{a,b,c}, Niels Voigt^{b,c,d}, Viacheslav O. Nikolaev^{e,j}, Stephan E. Lehnart^{a,b,c,k,*}

^a Cellular Biophysics and Translational Cardiology Section, Department of Cardiology & Pneumology, Heart Research Center Göttingen, University Medical Center Göttingen, Göttingen, Germany

^b DZHK (German Centre for Cardiovascular Research), partner site Göttingen, Germany

^c Cluster of Excellence "Multiscale Bioimaging: from Molecular Machines to Networks of Excitable Cells" (MBExC), University of Göttingen, Germany

^d Institute of Pharmacology and Toxicology, Heart Research Center Göttingen, University Medical Center Göttingen, Göttingen, Germany.

^e Institute of Experimental Cardiovascular Research, University Medical Center Hamburg-Eppendorf, Hamburg, Germany

^f Department of Physics and Astronomy, University of Florence, Florence, Italy

^g European Laboratory for Non-Linear Spectroscopy and National Institute of Optics (INO-CNR), Sesto Fiorentino, Italy

^h Molecular Biology Division, Biomedical Research Foundation, Academy of Athens, Athens, Greece

ⁱ Institute for Experimental Cardiovascular Medicine, University Heart Center Freiburg, Faculty of Medicine, University of Freiburg, Freiburg im Breisgau, Germany

^j DZHK (German Centre for Cardiovascular Research), partner site Hamburg/Kiel/Lübeck, Germany

^k BioMET, Center for Biomedical Engineering and Technology, University of Maryland School of Medicine, Baltimore, MD, USA

ARTICLE INFO

Keywords:

Adenylyl cyclase
Atrial myocyte
cAMP
 Ca^{2+} signaling
FRET biosensor
Ryanodine receptor

ABSTRACT

Axial tubule junctions with the sarcoplasmic reticulum control the rapid intracellular Ca^{2+} -induced Ca^{2+} release that initiates atrial contraction. In atrial myocytes we previously identified a constitutively increased ryanodine receptor (RyR2) phosphorylation at junctional Ca^{2+} release sites, whereas non-junctional RyR2 clusters were phosphorylated acutely following β -adrenergic stimulation. Here, we hypothesized that the baseline synthesis of 3',5'-cyclic adenosine monophosphate (cAMP) is constitutively augmented in the axial tubule junctional compartments of atrial myocytes. Confocal immunofluorescence imaging of atrial myocytes revealed that junctin, binding to RyR2 in the sarcoplasmic reticulum, was densely clustered at axial tubule junctions. Interestingly, a new transgenic junctin-targeted FRET cAMP biosensor was exclusively co-clustered in the junctional compartment, and hence allowed to monitor cAMP selectively in the vicinity of junctional RyR2 channels. To dissect local cAMP levels at axial tubule junctions versus subsurface Ca^{2+} release sites, we developed a confocal FRET imaging technique for living atrial myocytes. A constitutively high adenylyl cyclase activity sustained increased local cAMP levels at axial tubule junctions, whereas β -adrenergic stimulation overcame this cAMP compartmentation resulting in additional phosphorylation of non-junctional RyR2 clusters. Adenylyl cyclase inhibition, however, abolished the junctional RyR2 phosphorylation and decreased L-type Ca^{2+} channel currents, while FRET imaging showed a rapid cAMP decrease. In conclusion, FRET biosensor imaging identified compartmentalized, constitutively augmented cAMP levels in junctional dyads, driving both the locally increased phosphorylation of RyR2 clusters and larger L-type Ca^{2+} current density in atrial myocytes. This cell-specific cAMP nanodomain is maintained by a constitutively increased adenylyl cyclase activity, contributing to the rapid junctional Ca^{2+} -induced Ca^{2+} release, whereas β -adrenergic stimulation overcomes the junctional cAMP compartmentation through cell-wide activation of non-junctional RyR2 clusters.

* Corresponding authors at: University Medical Center Göttingen, Robert-Koch-Str. 42a, 37075 Göttingen, Germany.

E-mail addresses: soeren.brandenburg@med.uni-goettingen.de (S. Brandenburg), slehnart@med.uni-goettingen.de (S.E. Lehnart).

<https://doi.org/10.1016/j.jmcc.2022.01.003>

Received 16 October 2021; Received in revised form 15 December 2021; Accepted 8 January 2022

Available online 13 January 2022

0022-2828/© 2022 The Authors. Published by Elsevier Ltd. This is an open access article under the CC BY-NC-ND license (<http://creativecommons.org/licenses/by-nc-nd/4.0/>).

1. Translational perspective

Cell type-specific atrial myocyte functions are key to understand the molecular pathomechanisms of atrial cardiomyopathy, promoting arrhythmias and stroke. In atrial myocytes, axial tubule junctions with the sarcoplasmic reticulum contain highly phosphorylated RyR2 channel clusters priming Ca^{2+} release. We show that junctin is locally concentrated in this atria-specific junctional compartment, locally and molecularly interacting with RyR2. In analogy, Epac1-JCN, a new transgenic cAMP-specific biosensor, co-localizes with junctional RyR2 clusters. Indeed, live-cell Epac1-JCN FRET imaging demonstrates constitutively increased junctional cAMP levels. Thus, augmented cAMP levels sustain the compartmentalized RyR2 phosphorylation. This newly discovered atria-specific cAMP nanodomain is directly relevant for future studies of atrial pathologies and furthermore for understanding of cAMP-targeted therapeutic interventions.

2. Introduction

In atrial myocytes (AMs), rapid intracellular Ca^{2+} signaling is controlled by cell-specific nanodomains namely extensive sarcolemmal axial tubule junctions with the sarcoplasmic reticulum (SR) [1]. Notably, similar network architectures predominantly composed of axial tubules were recently shown across mammalian species from mouse to human atria [2]. The atria-specific junctional Ca^{2+} release units are highly sensitive to Ca^{2+} -dependent activation at least in part due to a constitutively increased protein kinase A (PKA) and Ca^{2+} /calmodulin-dependent protein kinase II (CaMKII) phosphorylation of the junctional ryanodine receptor type 2 (RyR2) at Ser2808 and Ser2814, respectively [1]. In sharp contrast, non-junctional RyR2 clusters, representing the great majority of atrial Ca^{2+} release channels, exhibit a much lower or no PKA or CaMKII phosphorylation under non-stimulated baseline conditions [1]. For the biogenesis of the junctional membrane complex in AMs, the membrane-tethering SR protein junctophilin-2, despite its relatively low expression level, is highly concentrated in axial tubule junctions together with the highly PKA and CaMKII phosphorylated RyR2 channels, whereas very little non-junctional junctophilin-2 exists and clusters with co-localized RyR2 channels [3].

Previously, each of the L-type Ca^{2+} channel (LTCC) isoforms Cav1.2 and Cav1.3 were shown to be densely clustered in the axial tubule membranes in AMs, where they locally activate Ca^{2+} -induced Ca^{2+} release (CICR) upon membrane depolarization [1,2]. Both LTCC isoforms as well as RyR2 channels are regulated in macromolecular protein complexes in the junctional nanodomain through adenylyl cyclases that catalyze the synthesis of the second messenger 3',5'-cyclic adenosine monophosphate (cAMP) [4]. Although PKA and CaMKII were identified as the proximal kinases of the RyR2 substrate at axial tubule junctions, the atria-specific mechanism that underlies the constitutively increased junctional RyR2 phosphorylation at baseline in the absence of β -adrenergic stimulation is currently unknown [5].

Notably, CICR in AMs has been previously conceptualized as a slow Ca^{2+} signaling process described by U-shaped transversal Ca^{2+} transients based on a model of sparse or no T-tubules [6–8]. However, more recent studies established an alternative rapid CICR model in AMs based on extensive axial tubule junctions [1–3]. In this novel AM model, β -adrenergic stimulation additionally recruits Ca^{2+} release sites through cell-wide PKA phosphorylation of the non-junctional RyR2 channel complexes, significantly accelerating and amplifying atrial SR Ca^{2+} release [1,9]. Hence, in contrast to the constitutively increased phosphorylation of RyR2 clusters strictly at axial tubule junctions at baseline, β -adrenergic stimulation overcomes this junctional cAMP compartmentation through recruitment of additional non-junctional PKA phosphorylated RyR2 clusters and surrounding sarcomeres [1].

Previous studies further established the SR proteins calsequestrin-2, triadin and junctin as components of the quaternary macromolecular

RyR2 Ca^{2+} release channel complex [10]. Junctin provides the physiologically important interactions between calsequestrin-2 in the SR lumen and the RyR2 channel [11]. Interestingly, junctin knockout in the mouse heart leads to SR Ca^{2+} overload and enhanced cardiac contractility, but also increases ventricular automaticity [12]. However, the subcellular junctin functions have not been studied in AMs previously.

Here, we demonstrate the differential subcellular clustering of junctin in junctional versus non-junctional compartments in AMs in contrast to ventricular myocytes (VMs). Because the protein expression of junctin occurred at a $\sim 80\%$ lower atrial compared to the ventricular protein level, the atrial stoichiometric junctin/RyR2 ratio was significantly lower. While ventricular RyR2 clusters showed a high degree of junctin co-localization, atrial junctin was highly co-clustered with junctional but not with non-junctional RyR2 channels. Based on this atria-specific, differential subcellular junctin distribution, we developed a confocal imaging strategy to capture the local cAMP levels at baseline and pharmacological cAMP changes inside the atrial junctional nanodomains. Using the FRET cAMP biosensor Epac1 fused to the cytoplasmic N-terminus of junctin (Epac1-JCN) transgenically expressed in the mouse heart [13], we monitored the local junctional cAMP concentration changes at axial tubule junctions and peripheral subsurface Ca^{2+} release sites. Strikingly, constitutively increased baseline cAMP levels at axial tubule junctions in non-stimulated living AMs corresponded with an increased local adenylyl cyclase activity, driving both augmented LTCC currents and rapid local Ca^{2+} release flux through highly PKA phosphorylated RyR2 channels, jointly increasing CICR at axial tubules. Vice versa, pharmacological adenylyl cyclase inhibition acutely decreased the LTCC currents and abolished the junctional RyR2 cluster phosphorylation, unmasking a constitutively augmented dyadic cAMP synthesis priming high-gain CICR at axial tubule junctions in AMs under baseline conditions.

3. Methods

Additional information is provided in the **Supplementary Methods**.

3.1. Mouse cardiomyocytes

AMs and VMs were isolated from adult, 10–16 weeks old C57BL/6 N mouse hearts using collagenase type II (Worthington) in nominally Ca^{2+} free perfusion buffer as described [1,14]. Please refer to **Supplementary Table 1** for detailed information on the buffer compositions. Experimental inclusion of isolated cardiomyocytes was based on the following criteria independently of experimental grouping: intact cell surface boundary, regular sarcomeric striations, and transverse-axial tubule (TAT) network integrity. Cardiomyocytes showing apparent membrane defects such as disrupted TAT components or extracellular membrane clumps were excluded from further analyses. In this study, “empty” AMs devoid of TAT networks were not observed in the context of live-cell membrane or fixed-cell immunofluorescence imaging studies. The generation of the Epac1-JCN transgenic mouse model has been described previously in a parallel manuscript [13]. Epac1-camps mice were characterized previously [15]. Junctin knockout mice (*Asph^{-/-}*) were used to demonstrate the specificity of the junctin antibody by immunoblotting and immunostaining (Fig. 1A and **Supplementary Fig. 5A**) [12]. The generation of RyR2-S2808A^{+/+} knockin mice was described previously [9]. Mice were anesthetized with 2% isoflurane (AbbVie) in oxygen using an isoflurane vaporizer and induction chamber system (VisualSonics) prior to fast cervical dislocation. All animal procedures were performed in compliance with the guidelines from Directive 2010/63/EU of the European Parliament and following a registered IACUC protocol (no. T11.2).

3.2. Immunofluorescence microscopy

Isolated cardiomyocytes were fixed with 4% PFA on laminin-coated

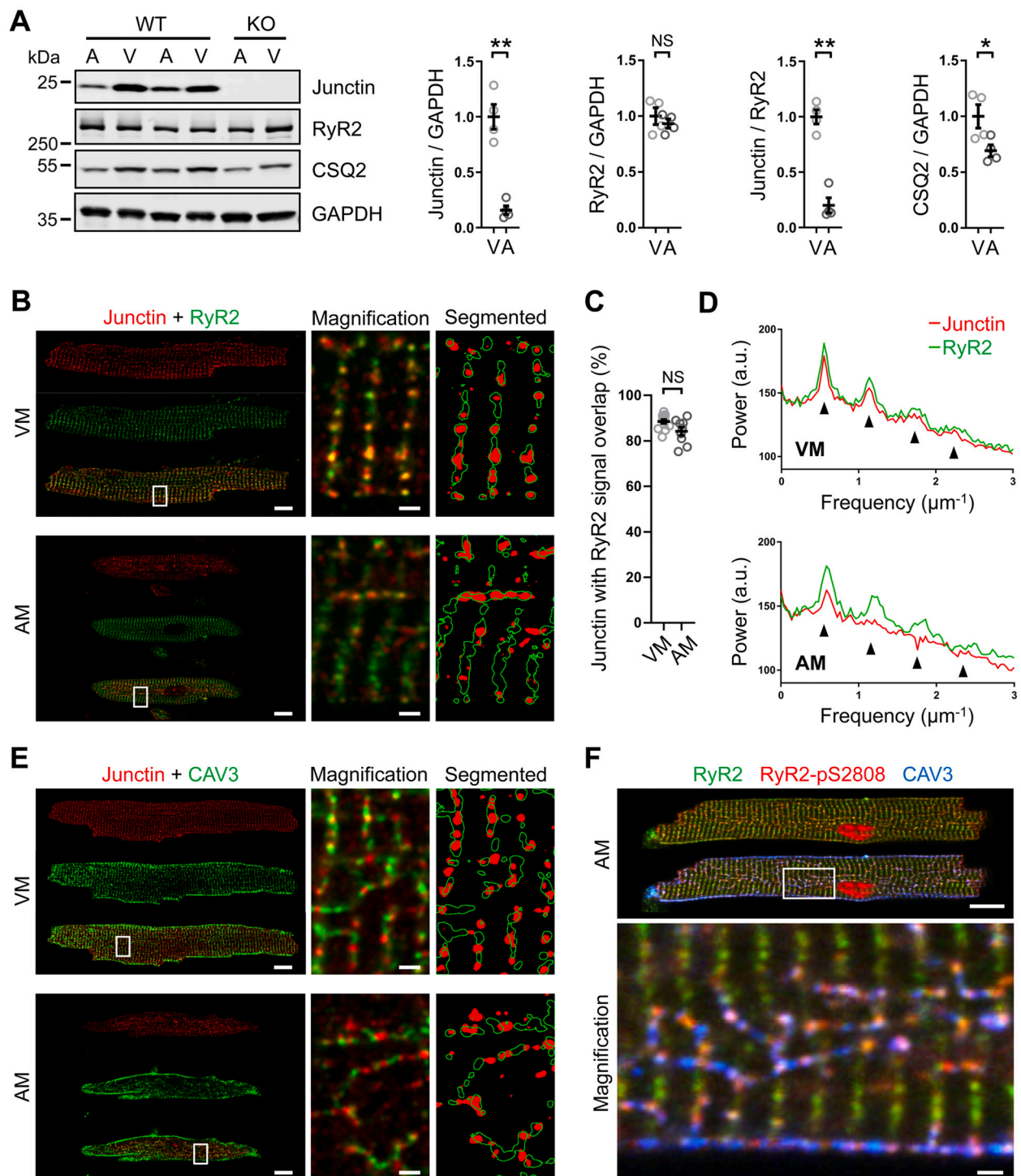


Fig. 1. Junctionin clusters at axial tubule junctions in atrial myocytes. (A) Junctin, ryanodine receptor (RyR2) and calsequestrin-2 (CSQ2) immunoblots of atrial (A) and ventricular (V) tissue lysates from wild-type (WT) versus junctin knockout (KO) mouse hearts. The atrial junctin protein expression was ~ 5-fold below the ventricular level. Paired data from $n = 4$ mouse hearts represented as dot plots; immunoblots are representative of three technical replicates. NS, not significant; $*p < 0.05$; $**p < 0.01$, Student's t -test. (B) Confocal co-immunostaining of junctin and RyR2 in ventricular (VM) versus atrial myocytes (AM). Whereas ventricular RyR2 clusters robustly co-localized with junctin as highlighted in the magnified and segmented image panels, axially aligned RyR2 clusters exclusively co-localized with junctin clusters in AMs. (C) Image segmentation dot plot showing a similar percentage of junctin cluster signals overlapping with RyR2 clusters in VMs and AMs. (D) Averaged *Fourier* power spectra showing the Z-line periodicity (arrowheads) of junctin signals in VMs but not in AMs, while the RyR2 signal periodicity was similar in AMs and VMs. $n = 9$ AMs and 14 VMs from 3 hearts in C and D. Unpaired Student's t -test. (E) Co-immunostaining of junctin and caveolin-3 (CAV3). Image segmentation confirmed that junctin clustering occurs at transverse tubule junctions in VMs, while in AMs junctin clusters are mainly associated with axially oriented tubules. (F) Triple AM immunostaining of RyR2, PKA-phosphorylated RyR2-Ser2808 (RyR2-pS2808) and CAV3 showing highly phosphorylated RyR2 clusters at axial tubules (blue), where junctin and RyR2 are co-localized (yellow). Immunostaining images in B, E and F are representative of at least three cell isolations from individual mouse hearts. White boxes indicate magnified regions. Scales indicate 10 μm (whole cell) or 1 μm (magnification). (For interpretation of the references to colour in this figure legend, the reader is referred to the web version of this article.)

coverslips, permeabilized with blocking buffer (0.2% Triton, 10% bovine calf serum in PBS) and incubated with the primary antibodies at 4 °C overnight. The detailed antibody information is provided in **Supplementary Table 2**. Following three washing steps with blocking buffer, secondary antibodies coupled to the fluorophores STAR635P, STAR580 or STAR488 (Abberior) were added at a dilution of 1:1000 for 2 h at room temperature. Subsequently, the samples were washed three times with PBS and mounted on glass coverslips in mounting medium. Confocal images were acquired using a Leica TCS SP8 microscope with a HC PL APO C2S 100×/1.40 oil objective and processed in ImageJ/Fiji (<https://imagej.net/Fiji>).

3.3. Live-cell FRET imaging

Isolated AMs and VMs were used for FRET measurements by epifluorescence microscopy as described before [16]. Furthermore, for confocal FRET imaging, isolated myocytes were incubated with 1 μM Chol-PEG-KK114, custom-synthesized as described [2], in perfusion buffer for 10 min on laminin-coated imaging chambers and subsequently washed. Confocal images were acquired with a Zeiss LSM 880 microscope using a Plan-Apochromat 63×/1.40 oil objective with a pixel size of 100 × 100 nm. For confocal FRET measurements, four channels were acquired: 1) YFP (excitation 514 nm, emission 550–600 nm), 2) CFP (excitation 405 nm, emission 450–500 nm), 3) YFP-FRET (excitation 405 nm, emission 550–600 nm) and 4) Chol-PEG-KK114 (excitation 633 nm, emission 650–700 nm). All channels were acquired using a laser power of 2%, 16× line averaging and a pixel dwell time of 400 ns. All FRET experiments were performed in freshly prepared perfusion buffer at room temperature. For pharmacological treatment, cells were exposed to final concentrations of 100 nM isoproterenol (I6504, Sigma-Aldrich), 10 μM forskolin (F3917, Sigma-Aldrich), 100 μM MDL-12,330A (M182, Sigma-Aldrich), 300 μM NKY80 (N2165, Sigma-Aldrich), and 100 μM SQ22,536 (S153, Sigma-Aldrich). If not stated otherwise, controls imply treatment with carrier solution.

3.4. Combined voltage-clamp and FRET measurements

Simultaneous FRET and LTCC current measurements were performed in Epac1-JNC AMs using the whole-cell ruptured patch-clamp technique at 37 °C and voltage-clamp. LTCC currents were normalized to the membrane capacitance and displayed as current density (pA/pF). 10 μmol/L of MDL, solved in Barium-4-AP solution, was applied with a pressurized flow perfusion system after the baseline peak LTCC current and the FRET emission ratio had reached steady-state, simultaneously.

3.5. Combined axial tubule and Ca²⁺ imaging

Confocal intracellular Ca²⁺ imaging in freshly isolated AMs using Fluo4-AM in Tyrode's solution was combined with live-cell membrane labelling using 1 μM Chol-PEG-KK114 as described previously [2], or 40 μM di-8-ANEPPS (Thermo Fischer Scientific). Images were acquired using a Zeiss LSM 880 microscope with a Plan-Apochromat 63×/1.40 oil objective and a pixel size of 100 × 100 nm.

3.6. STED imaging

For STED superresolution imaging of TAT membrane structures in Epac1-JNC transgenic AMs (Fig. 2E) and triple-immunostainings (Fig. 2F and G), we used a Leica TCS SP8 system with a HC PL APO C2S 100×/1.40 oil objective and a pixel size of 16.23 × 16.23 nm. Please refer to **Supplementary Fig. 1** for detailed information regarding point spread function and in situ resolution in confocal and STED imaging modalities.

3.7. Random access multi-photon (RAMP) microscopy

Action potentials before and after MDL incubation were recorded by RAMP imaging simultaneously at different subcellular membrane structures in AMs as described previously [17,18]. Measurements were performed in nominally Ca²⁺ free buffer solution (**Supplementary Table 1**) to preserve cell viability.

3.8. Immunoblot protein analysis

For protein analysis, atrial and ventricular tissue samples were prepared from the same mouse hearts as described previously [1]. All primary antibodies used are listed in **Supplementary Table 2**, full gels are provided as **Supplementary Figs. 2 and 3**.

3.9. Data availability

The data underlying this article will be shared on reasonable request to the corresponding authors.

3.10. Statistics

Statistical analysis was performed in Microsoft Excel 2010, Graphpad Prism 7.03 and OriginPro 8.5. Normal distribution was tested by the Shapiro-Wilk test. Statistical difference of variables in normal distribution between two groups was tested using the 2-tailed Student's *t*-test. Datasets from paired experiments including pharmacological modulation were tested pairwise as indicated in the figure legends. One-way ANOVA with post-hoc Tukey test was used for testing parameters in normal distribution between three or more groups. To test for statistical difference between two groups of non-normal frequency distribution (Fig. 5C, **Supplementary Fig. 12C**, **Supplementary Fig. 15B**), we utilized the non-parametric Mann-Whitney *U* test. Unless indicated otherwise, data are presented as mean ± SEM. *P*-values <0.05 were accepted to indicate statistical difference.

4. Results

4.1. Local junctin clustering at axial tubule junctions of atrial myocytes

While junctin is encoded by the *Asph* gene, alternative splicing generates four distinct proteins [19]. Using a custom-made antibody raised against a unique C-terminal junctin epitope, immunoblotting of paired atrial and ventricular tissue lysates from wild-type versus junctin knockout *Asph*^{−/−} hearts confirmed a junctin-specific signal at ~ 25 kDa (Fig. 1A and **Supplementary Fig. 2**) [12]. Unexpectedly, in myocardial tissue lysates the atrial compared to the ventricular junctin expression level was approximately five times lower, while RyR2 expression was similar, resulting in a significantly reduced atrial junctin/RyR2 protein ratio (Fig. 1A). In contrast, the protein expression level of the alternatively spliced aspartyl/asparaginyl β-hydroxylase (ASPH), detected as the major *Asph* proteoform at ~ 100 kDa, was five times higher in atrial compared to ventricular tissue lysates (**Supplementary Fig. 4**). Interestingly, and previously unknown, the atrial compared to the ventricular mouse calsequestrin-2 expression level was 31 ± 4.6% lower (Fig. 1A). Therefore, we wondered how CICR in AMs can be maintained through the tetrameric RyR2 channel complex despite the considerably decreased junctin and calsequestrin-2 stoichiometric protein levels.

Confocal co-immunofluorescence imaging in adult VMs isolated from mouse hearts showed a high degree of co-localization between junctin and RyR2 in transverse sarcomeric striations (Fig. 1B, *top image panels*), and image segmentation confirmed this co-localization (Fig. 1B, *top segmented*). In sharp contrast, AMs stained with the same antibodies revealed larger junctin clusters mainly distributed along axially oriented RyR2 clusters, whereas most of the RyR2 clusters in transverse striations showed no or only weak junctin signals (Fig. 1B, *bottom image panels*).

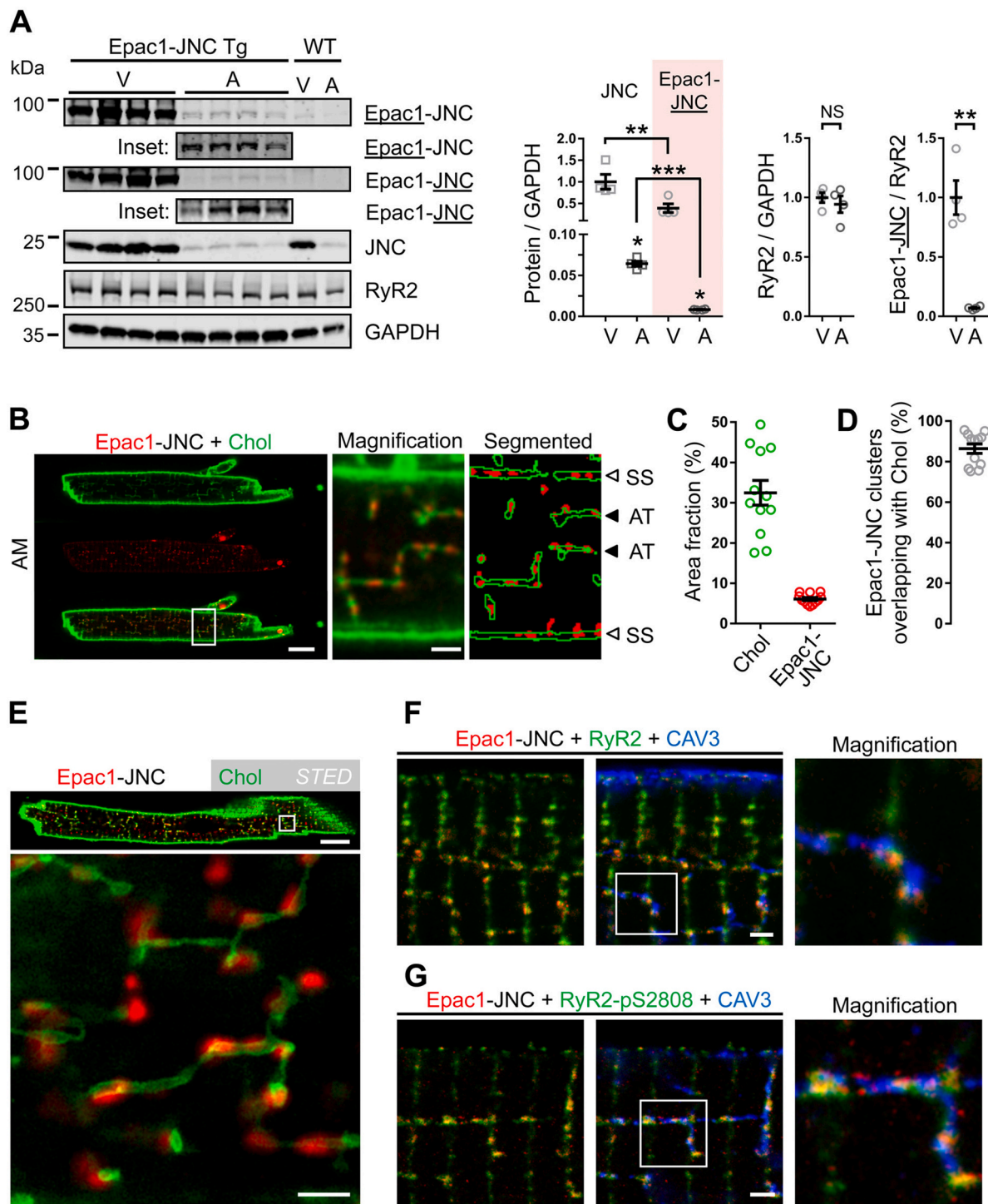


Fig. 2. Atrial Epac1-JCN biosensor protein level and subcellular distribution. (A) Immunoblotting revealed significantly lower atrial compared to ventricular transgenic Epac1-JNC levels, and a significantly lower atrial Epac1-JCN/RyR2 ratio. Epac1-JNC was detected both by anti-YFP (Epac1-JNC) and anti-junctional immunoblotting (Epac1-JNC) as indicated. Paired data from $n = 4$ Epac1-JNC hearts represented as dot plots; immunoblots are representative of three technical replicates. NS, not significant; $**p < 0.01$, $***p < 0.001$, Student's t -test. (B) Combined live-cell confocal imaging of Epac1-JNC via YFP excitation (red) and TAT membranes using $1 \mu\text{M}$ Chol-PEG-KK114 (Chol, green) in atrial myocytes. The magnified and segmented panels show Epac1-JNC clusters at axial tubule (AT) or subsurface (SS) sites. (C) Whereas the area fraction of TAT membrane signals amounts to 33%, the Epac1-JNC fraction amounts to 6%. (D) Nearly 90% of Epac1-JNC clusters overlap with intact TAT membrane structures in living AMs. $n = 12$ AMs from 3 mouse hearts for C and D. (E) Live-AM confocal imaging of the Epac1-JNC clusters' YFP signal (red) combined with STED nanoscopy of TAT membranes (Chol, $1 \mu\text{M}$, green). The magnified panel shows large Epac1-JCN clusters tightly abutting the junctional cytosolic surface of membrane tubules. (F-G) Triple-colour STED imaging of Epac1-JNC clusters in AMs: (F) anti-YFP immunostaining of Epac1-JNC clusters co-localized with RyR2 clusters (yellow) alternating with caveolin-3 (CAV3) at axial tubule structures (blue). (G) Epac1-JNC signals overlapping with highly Ser2808 phosphorylated junctional RyR2 clusters (yellow) at TAT components (blue). Immunostaining images in F and G are representative of three cell isolations from individual mouse hearts. Scale bars $1 \mu\text{m}$. White boxes indicate magnified regions. (For interpretation of the references to colour in this figure legend, the reader is referred to the web version of this article.)

Image segmentation confirmed larger junctin cluster signals mainly overlapping with RyR2 clusters in longitudinal but much less in transversal signal patterns (Fig. 1B, *bottom segmented*). A co-localization analysis showed that the junctin cluster signals, despite the differential subcellular protein distribution and low expression level, highly overlapped with RyR2 clusters in both VMs and AMs (Fig. 1C). To proof the specificity of the junctin cluster signals labelled by the primary antibody, we excluded any unspecific antibody signals in isolated myocytes from junctin knockout *Asph^{-/-}* mouse hearts (**Supplementary Fig. 5A**), furthermore confirming a preserved signal pattern of the atrial RyR2 cluster arrangements similar to wild-type cardiomyocytes in atrial tissue sections (**Supplementary Fig. 6**) [12]. To further characterize the subcellular junctin and RyR2 cluster signals, a fast Fourier transform (FFT) algorithm analyzed the periodicity each of the junctin and RyR2 signals in transverse striations (Fig. 1D). In VMs, the junctin and RyR2 signals showed the expected co-localized signal periodicity (Fig. 1D, *top*). However, in AMs the RyR2 signal periodicity was robustly reproduced, whereas the junctin power peaks were barely visible, in line with a decreased transversal signal periodicity (Fig. 1D, *bottom*).

Recently, a new physiological model of rapid atrial excitation-contraction coupling was proposed, where junctional, highly phosphorylated RyR2 clusters at axial tubules activate rapid intracellular Ca^{2+} release deep inside AMs [1]. Hence, we wondered if junctin also predominantly clusters in axial tubule junctions. As expected, isolated VMs co-immunostained for junctin and caveolin-3, the latter a marker of transverse-axial tubule (TAT) and surface membrane structures, showed a large signal overlap of junctin clusters mainly at transverse tubules (Fig. 1E, *top image panels*). Image segmentation confirmed the major overlap of the junctin cluster signals with the transverse tubule signals (Fig. 1E, *segmented*). In contrast, although junctin is anchored in the SR membrane and cannot physically bridge the dyadic gap [19], we observed large junctin cluster signals mainly near caveolin-3 labelled axial tubules in AMs (Fig. 1E, *bottom image panels*). Image segmentation confirmed the local association between junctin clusters at axial tubules interspersed laterally by caveolin-3 signals (Fig. 1E, *segmented*). Thus, despite a profoundly lower protein expression in the atria, the junctin signals were highly co-clustered with the RyR2 signals at axial tubules in AMs, whereas non-junctional RyR2 clusters showed no or only weak junctin signal co-localization.

Finally, using a triple immunostaining approach, we confirmed that the RyR2 clusters at axial tubules are highly phosphorylated at Ser2808 at baseline in untreated AMs (Fig. 1F), consistent with an earlier study demonstrating the signal specificity of phospho-Ser2808 labelling through phospho-site specific Ser2808Ala-knockin ablation (**Supplementary Fig. 5B**) [1]. Hence, we hypothesized that the atrial junctin clusters in the dyadic compartment are exposed to a constitutively increased activity of the cAMP-regulated PKA catalytic subunit. To test this hypothesis, we investigated transgenic AMs from mouse hearts, expressing the FRET-based cAMP biosensor Epac1-camps targeted to the junctin N-terminus (Epac1-JNC), to directly detect the local cAMP concentration changes in axial tubule junctions [13].

4.2. Junctin-targeted cAMP FRET biosensor localization in axial tubule junctions in atrial myocytes

The recently established transgenic Epac1-JNC mouse model overexpresses the FRET-based cAMP biosensor Epac1-camps as N-terminal junctin-targeted fusion protein under control of the α -myosin heavy chain promoter in VMs [13]. Immunoblotting of atrial tissue lysates from wild-type versus Epac1-JNC hearts confirmed preserved native junctin, RyR2, junctophilin-2, SR Ca^{2+} -ATPase SERCA2a, phospholamban and calsequestrin-2 expression levels, and excluded baseline changes in RyR2 phosphorylation at Ser2808 (**Supplementary Fig. 7**). Interestingly, transgenic mouse heart lysates showed a significantly lower atrial versus ventricular expression of the fusion protein Epac1-JNC based on anti-junctin immunoblotting (Fig. 2A, *left*). Apparently,

this relative atrio-ventricular Epac1-JNC expression difference was qualitatively analogous to the endogenous junctin expression difference (Fig. 2A, *protein/GAPDH*). Importantly, in atrial tissue lysates the transgenic Epac1-JNC protein expression level amounted to only $13 \pm 0.4\%$ relative to the endogenous junctin level (Fig. 2A, *protein/GAPDH*). This result confirmed a ~ 8 -fold lower atrial Epac1-JNC compared to native junctin expression level, minimizing the risk of overexpression artefacts in transgenic AMs. Consequently, since the RyR2 protein level was not changed in atrial versus ventricular tissue, the atrial Epac1-JNC/RyR2 ratio was also significantly lower amounting to only $7 \pm 0.6\%$ as compared to the ratio in ventricular tissue (Fig. 2A, *right*). Finally, co-immunoprecipitation experiments revealed a protein-protein interaction between RyR2 with both endogenous junctin and transgenic Epac1-JNC in atrial tissue lysates (**Supplementary Fig. 8A**). Notably, the Epac1-JNC interaction with RyR2 did not compromise the interaction with the endogenous junctin protein, as confirmed by a preserved JNC/RyR2 ratio (**Supplementary Fig. 8B**).

Next, we sought to analyze the subcellular Epac1-JNC biosensor distribution in living isolated AMs from transgenic mice. Using live-cell confocal microscopy, Epac1-JNC was localized by YFP excitation, while the custom-synthesized cholesterol dye Chol-PEG-KK114 (1 μM) labelled the extracellular membrane leaflet based on a protocol established previously (Fig. 2B, *left*) [2]. In magnifications, AMs from Epac1-JNC hearts showed the typical cell-specific TAT endomembrane network mainly composed of axial tubule and rare transverse tubule components, the latter connecting the intracellular axial tubule structures with the lateral surface sarcolemma cell-wide as confirmed in image stacks and 3D reconstructions (**Supplementary Fig. 9**) [1–3]. Interestingly, axial tubules may be directly connected to the intercalated disc's membrane folds (**Supplementary Fig. 9**). While quantitatively the intracellular TAT network in Epac1-JNC AMs mainly consisted of AT components, this was further consistent with a preserved TAT network architecture and density similar to wild-type AMs (**Supplementary Fig. 10**) [2]. Importantly, the Epac1-JNC biosensor signals clearly showed a highly clustered pattern directly overlapping the intracellular TAT network signals and the outer surface sarcolemma (Fig. 2B, *magnification*). To quantify the percentage of Epac1-JNC signals overlapping with Chol-PEG-KK114 stained membrane structures, the fluorescent live-cell signals were segmented by local thresholding (Fig. 2B, *segmented*). While the Chol-PEG-KK114 membrane signals covered $32 \pm 2.9\%$ of the total cell area, the Epac1-JNC signals covered a much smaller area fraction of only $6 \pm 0.4\%$ (Fig. 2C). Importantly, despite its low area fraction, $86 \pm 2.2\%$ of the Epac1-JNC signals overlapped with TAT or surface membrane signals in living AMs (Fig. 2D).

In addition, we used STimulated Emission Depletion (STED) nanoscopy for live-cell superresolution imaging of Epac1-JNC in AMs stained with Chol-PEG-KK114. While STED significantly increases the contrast and resolution of the Chol-PEG-KK114 stained intact membrane signals as reported previously [2], the visualization of the Epac1-JNC biosensor by YFP STED imaging was moderately improved (**Supplementary Fig. 11**) [20]. Finally, combining confocal Epac1-JNC with STED-based Chol-PEG-KK114 imaging, we confirmed the particularly frequent clustering of the biosensor molecules at membrane contact sites along axial tubules in living AMs (Fig. 2E). Triple co-immunofluorescence STED imaging of transgenic AMs further showed that the local Epac1-JNC signals alternated with caveolin-3 clusters at TAT membrane structures and co-localized with the axially distributed RyR2 clusters (Fig. 2F). A subcellular analysis of triple-immunostained transgenic AMs confirmed an overall similar local Epac1-JNC biosensor expression at TAT-associated versus subsurface junctional RyR2 clusters (**Supplementary Fig. 12**). In addition, Epac1-JNC AMs demonstrated a preserved local signal pattern of the highly Ser2808 phosphorylated RyR2 clusters at the caveolin-3 labelled TAT network and surface membrane similar to the pattern expected in wild-type AMs reported previously (**Supplementary Fig. 13**) [1,2]. Finally, the highly Ser2808 phosphorylated RyR2 clusters overlapped with the immunostained Epac1-JNC

cluster signals at axial tubules indicated by caveolin-3 cluster signals (Fig. 2G).

4.3. Cell-wide and subcellular Epac1-JNC FRET imaging resolves spatiotemporal cAMP signaling

Based on the selective Epac1-JNC clustering in junctional compartments, we studied the baseline versus pharmacologically induced changes of the junctional cAMP concentration in living AMs compared to VMs (Fig. 3A). As expected, β -adrenergic stimulation of VMs by isoproterenol (100 nM) resulted in a rapid decrease of the FRET ratio consistent with an acutely increased cAMP synthesis in the junctional compartments as shown by epifluorescence FRET imaging

(Supplementary Fig. 14A). Next, treatment of VMs with the adenylyl cyclase agonist forskolin (10 μ M) saturated the FRET ratio decrease consistent with a maximally stimulated cAMP generation (Supplementary Fig. 14A). In analogy, isoproterenol followed by forskolin treatment in AMs successively and robustly decreased the FRET ratio consistent with an acutely increased cAMP synthesis in the junctional compartments (Fig. 3B). However, in AMs as compared to VMs apparently each the isoproterenol and the forskolin treatment steps resulted in a less pronounced decrease of the FRET ratio, suggesting quantitative differences in the extent of junctional cAMP synthesis.

Vice versa, incubation of VMs with the adenylyl cyclase inhibitor MDL12,330A (MDL, 100 μ M) resulted in a moderate FRET increase, indicating a decrease in cAMP synthesis (Supplementary Fig. 14B). In

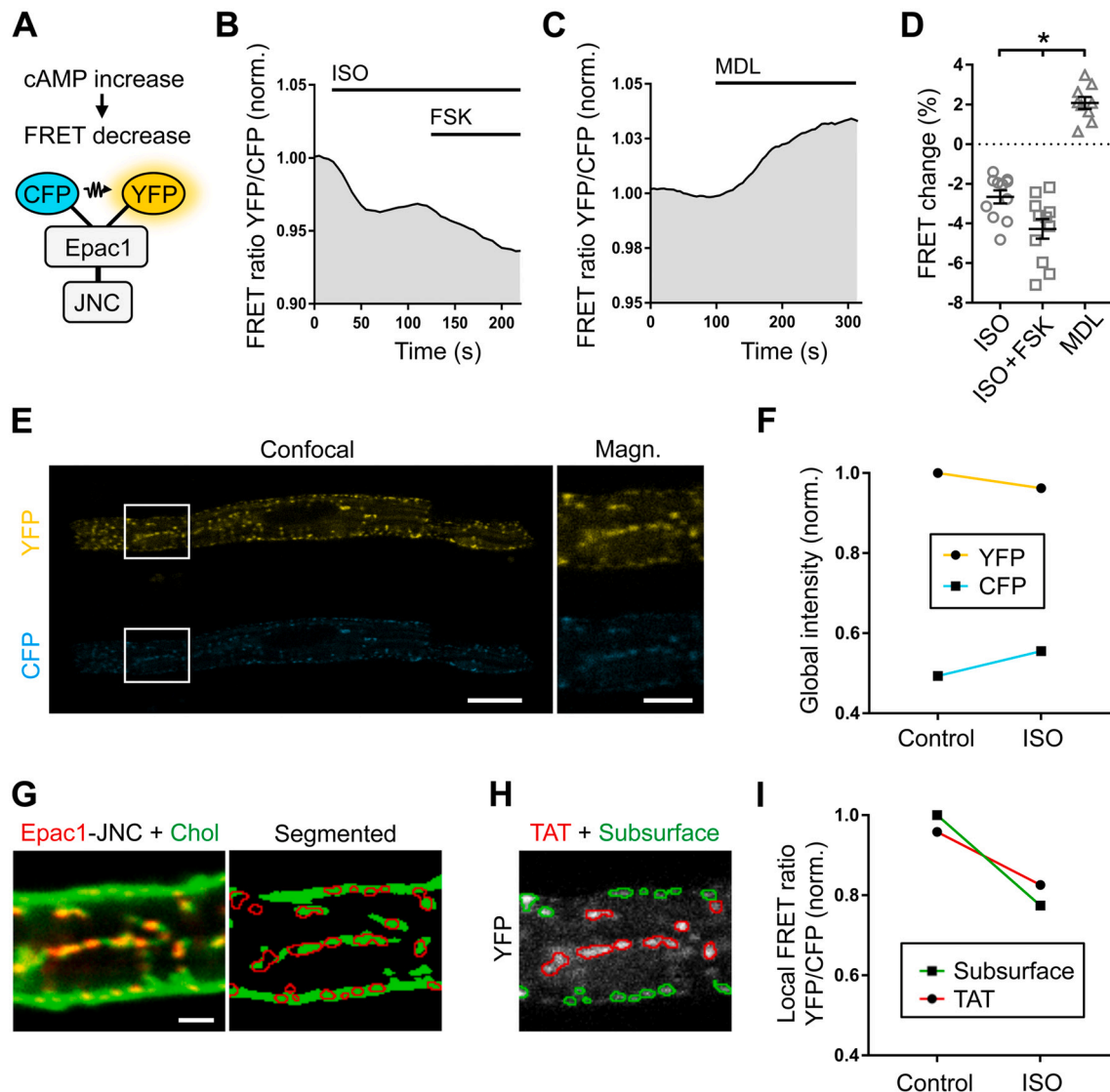


Fig. 3. Atrial myocyte FRET imaging and subcellular cAMP compartment analysis. (A) Cartoon showing the junctin-targeted transgenic Epac1-JNC FRET biosensor. Increased cAMP levels decrease the FRET ratio. (B–C) Representative epifluorescence imaging FRET traces in Epac1-JNC transgenic AMs. (B) While each isoproterenol (ISO 100 nM) and forskolin (FSK 10 μ M) rapidly stimulated cAMP synthesis apparent as FRET ratio decreases, (C) adenylyl cyclase inhibition with MDL-12,330A (MDL 100 μ M) depressed cAMP synthesis evident as FRET ratio increase. (D) Dot plot summarizing the percentage FRET ratio change represented in B and C. $n = 11$ AMs ISO/FSK and 9 AMs MDL, each from 4 mouse hearts. * $p < 0.05$, 1-way ANOVA. (E–I) Scheme of a the newly developed confocal FRET imaging approach: (E) confocal AM imaging of Epac1-JNC clusters excited at 405 nm confirming both CFP and YFP signals at baseline. White boxes indicate magnified regions. (F) Global cell-wide intensity changes after ISO stimulation (100 nM, 90 s) confirming a reciprocal YFP decrease versus CFP signal increase during increased cAMP synthesis. (G) YFP excitation at 514 nm, membrane labelling by Chol-PEG-KK114 (Chol), and image segmentation (H) identify Epac1-JNC clusters in subsurface versus intracellular TAT membrane structures. (I) Line dot plot confirming the local FRET ratio decrease during ISO stimulation (100 nM, 90 s) both at subsurface and TAT sites. Scale 10 μ m (whole cell) or 2 μ m (magnification). (For interpretation of the references to colour in this figure legend, the reader is referred to the web version of this article.)

contrast to MDL, however, neither the adenylyl cyclase inhibitor NKY80 (300 μ M) nor SQ22,536 (100 μ M) increased the FRET ratio during the extended 5 min observation period (**Supplementary Figs. 14C–D**; please refer to the **Discussion** section for details). Importantly, AMs treated with MDL showed a pronounced increase of the FRET ratio consistent with a robust decrease in junctional cAMP generation (**Fig. 3C**). As the MDL-treated AMs were not exposed to any cAMP synthesis stimulating compounds (**Supplementary Table 1**), the MDL treatment apparently diminished the baseline cAMP synthesis in the junctional compartments consistent with a constitutively increased activity of the adenylyl cyclase enzymes. Indeed, in AMs the average FRET change following isoproterenol and forskolin stimulation versus MDL inhibition were significantly decreased versus increased, respectively (**Fig. 3D**), confirming the pharmacologically modulated junctional cAMP synthesis. Taken together, the FRET ratio increase in Epac1-JCN expressing AMs following MDL treatment uncovered a robust junctional cAMP decrease, indicating a constitutively increased baseline activity of the adenylyl cyclase enzymes presumably in the junctional compartments.

Interestingly, as compared to the soluble cytosolic Epac1-camps FRET biosensor each in AMs and VMs (**Supplementary Fig. 14E–F**), the junction-targeted Epac1-JCN biosensor showed a pronounced change upon MDL treatment both in AMs and VMs (**Fig. 3C–D** and **Supplementary Fig. 14B**). Additionally, an analysis of the baseline FRET ratio in cardiomyocytes expressing the soluble Epac1-camps biosensor revealed a small, but significantly increased intracellular cAMP concentration in untreated AMs compared to VMs (**Supplementary Fig. 14G**), in line with constitutively increased cytosolic cAMP concentrations in AMs.

To assess the constitutively increased cAMP levels in the predominant axial tubule junctions, we developed a confocal imaging approach to directly resolve the Epac1-JCN FRET signals locally in AMs (**Supplementary Methods, Confocal FRET measurements**). Indeed, confocal FRET imaging detected the expected inverse CFP versus YFP signal changes during 90 s isoproterenol stimulation (**Fig. 3E–F**). Hence, the CFP and YFP fluorescence intensity changes confirmed the functionality of the Epac1-JCN biosensor under the given confocal live-cell imaging conditions. For confocal FRET-based image analysis, a correction factor was experimentally determined based on measuring the degree of CFP bleedthrough into the YFP-FRET channel in CFP plasmid transfected HEK293A cells (**Supplementary Fig. 14H**) [16]. Moreover, in living transgenic AMs labelled with Chol-PEG-KK114, confocal imaging showed both the intracellular TAT network and lateral surface membrane, where Epac1-JCN clusters were localized upon YFP excitation (**Fig. 3G, left**). Image segmentation confirmed the specific localization of the Epac1-JCN clusters both at axial tubules and the surface membrane (**Fig. 3G, right**; please see **Supplementary Methods** for detailed protocol information). Finally, Epac1-JCN clusters located in dyadic junctions at the central intracellular TAT network versus the peripheral subsurface membrane were dissected by subclassification analysis (**Fig. 3H**). Comparing the baseline versus 90 s isoproterenol stimulated Epac1-JCN cluster signals, the FRET signal ratio was acutely decreased both at the TAT and subsurface junctions (**Fig. 3I**). These results demonstrated an acute increase of the cAMP concentration in the junctional compartments following isoproterenol treatment. Notably, despite the relatively low biosensor expression level in AMs, confocal imaging combined with local cluster-based Epac1-JCN signal analysis improved the dynamic range of the captured FRET changes as compared to cell-wide epifluorescence imaging (compare **Fig. 3B** to **Fig. 3I**).

4.4. Constitutively increased cAMP levels in atrial junctional compartments

To demonstrate constitutively increased junctional cAMP pools in living AMs, acute treatment with the pan-inhibitory compound MDL was applied to interrogate the baseline activity of the adenylyl cyclase

isoforms in AMs. Confocal Epac1-JCN and TAT membrane imaging resolved the subcellular biosensor cluster locations at junctional compartments (**Figs. 4A, top**). Next, magnified colour-encoded 2D (**Fig. 4A, center**) and pseudo-3D surface plots (**Fig. 4A, bottom**) visualized the local YFP-FRET signal changes of subcellular Epac1-JCN clusters at exemplary axial tubules before versus 6 min after adenylyl cyclase inhibition by MDL (100 μ M). Apparently, the MDL treatment increased the local intensity of the YFP-FRET signal peaks at axial tubule junctions (**Fig. 4A, bottom**). Interestingly, subcellular analysis of the Epac1-JCN cluster signals demonstrated a significantly lower FRET ratio under untreated baseline conditions at junctional TAT as compared to the peripheral subsurface membrane sites (**Fig. 4B, control**). Hence, the latter result supports a constitutively increased cAMP level throughout the junctional TAT compartments. In contrast, adenylyl cyclase inhibition by MDL significantly increased the FRET ratio both at the junctional subsurface and intracellular TAT network sites (**Fig. 4B, MDL**), unmasking the increased local cAMP synthesis by the adenylyl cyclases at both subcellular compartment classes.

While the subsurface and TAT compartments responded similarly robust to the acute MDL inhibition, the observed baseline difference of the FRET ratio was statistically diminished by MDL, persisting only as a non-significant trend (**Fig. 4B**). Accordingly, the MDL-dependent FRET ratio change at junctional subsurface versus TAT sites was not significantly different (**Fig. 4C**). Nonetheless, despite this robust FRET effect in AMs, MDL may not completely inhibit the endogenous adenylyl cyclase activity given that pleiotropic and differentially expressed isoforms may exist in AMs [21].

Importantly, we confirmed the significantly lower FRET ratio under baseline conditions at junctional TAT compared to peripheral subsurface Epac1-JCN cluster sites in a second independent AM dataset (**Fig. 4D, control**). When these AMs were stimulated with isoproterenol (100 nM), the FRET ratio was significantly decreased both at junctional subsurface and TAT Epac1-JCN biosensor cluster sites (**Fig. 4D, ISO**). Finally, the percentage change of the ISO-stimulated FRET ratio at junctional subsurface versus intracellular TAT sites was not significantly different (**Fig. 4E**). Thus, the observed reciprocal MDL versus isoproterenol induced FRET changes are consistent with a locally compartmentalized and constitutively increased junctional adenylyl cyclase activity, sustaining the high cAMP levels both in the dyadic compartments of the TAT network and the subsurface membrane of AMs.

4.5. MDL inhibits the constitutive junctional RyR2 channel phosphorylation in atrial myocytes

As PKA phosphorylation of Ser2808 increases the open probability of RyR2 channels in VMs [22], we sought to investigate the post-translational effects of adenylyl cyclase inhibition in situ in the junctional membrane complexes of AMs. Firstly, phospho-epitope specific co-immunostaining confirmed prominent RyR2 cluster signals that were highly Ser2808 phosphorylated (RyR2-pS2808) at caveolin-3 labelled axial tubules, whereas non-junctional RyR2 clusters showed only weak background signals in transverse striations in untreated wild-type AMs (**Fig. 5A, control**). In contrast, MDL treatment (100 μ M) for 30 min completely diminished the junctional RyR2-pS2808 cluster signals at axial tubules in AMs (**Fig. 5A, MDL**). Secondly, co-immunostaining of the RyR2 substrate and the PKA target epitope RyR2-pS2808 explored the signal range of the Ser2808 phosphorylated clusters based on previously established workflows [1]. Under baseline control conditions, this confirmed the highly Ser2808 phosphorylated and mainly axially aligned junctional RyR2 clusters, regularly intersecting the more frequent but less or not phosphorylated RyR2 clusters in transverse striations (**Fig. 5B, control**). In contrast, 2 min isoproterenol stimulation (100 nM) maximally increased the transversal RyR2-pS2808 cluster signals (*yellow-to-white range*) throughout the cell (**Fig. 5B, ISO**), confirming the dynamic β -adrenergic in situ RyR2 channel regulation reported previously [1]. In sharp contrast, MDL treatment robustly

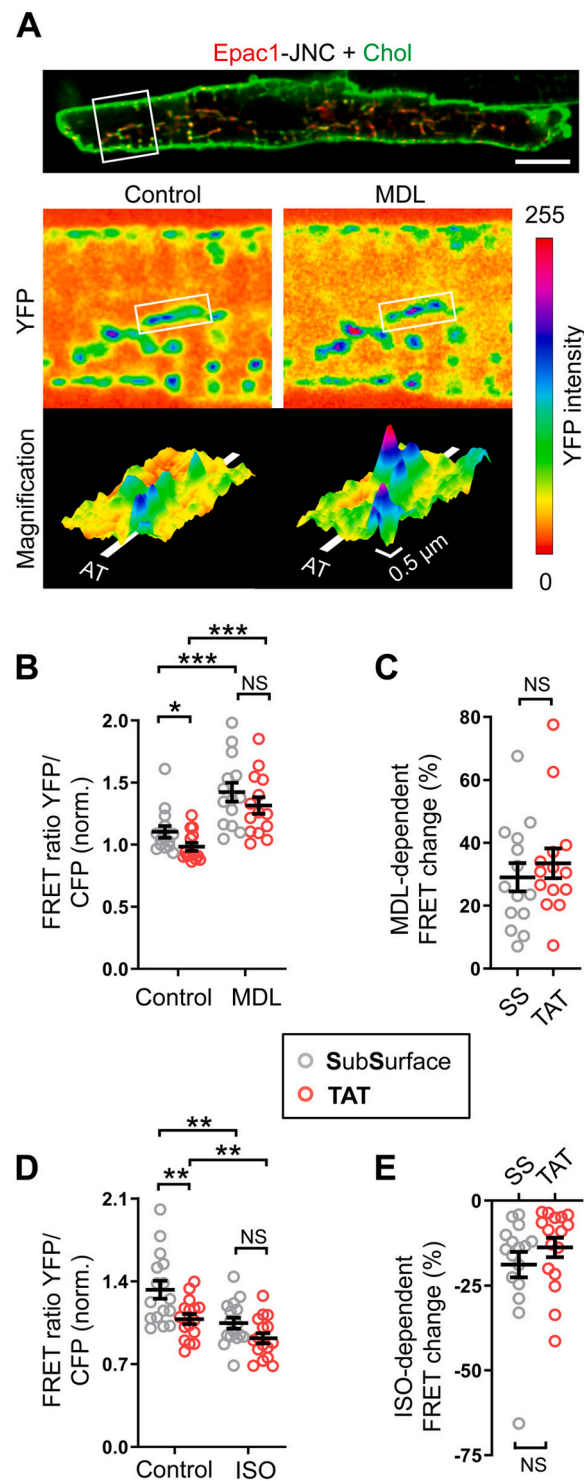


Fig. 4. Confocal cAMP compartment monitoring at axial tubule junctions in atrial myocytes. (A) Confocal Epac1-JNC cluster localization and local FRET imaging. *Top:* Representative AM image localizing Epac1-JNC clusters through YFP excitation (red) at intact intracellular membrane structures labelled by Chol-PEG-KK114 (Chol, green). The white boxes indicate the subsequently magnified AM regions. Scale 10 μ m. *Middle:* 2D representation showing the local changes in YFP-FRET intensity across the magnified AM section. *Bottom:* Local YFP-FRET intensity representation as pseudo-3D surface plots along an exemplary axial tubule (AT, axial direction indicated by white line). Compared to the baseline control (green-to-cyan) apparently the local intensity peaks are increased (cyan-to-red) after MDL treatment (100 μ M, 6 min). (B) Dot plot summarizing significant FRET ratio increases indicating a cAMP decrease after MDL treatment (100 μ M, 6 min) both at subsurface and TAT sites. (C) Dot plot excluding a significant MDL treatment-dependent FRET change between subsurface versus TAT sites. $n = 14$ AMs from 5 mouse hearts in B and C. (D) Dot plot confirming significant FRET ratio decreases consistent with a cAMP increase after ISO treatment (100 nM, 90 s) both at subsurface and TAT sites. (E) Dot plot excluding a significant ISO treatment-dependent FRET change between subsurface versus TAT sites. $n = 16$ AMs from 8 mouse hearts in D and E. NS, not significant; * $p < 0.05$, ** $p < 0.01$, *** $p < 0.001$, paired Student's t -test. (For interpretation of the references to colour in this figure legend, the reader is referred to the web version of this article.)

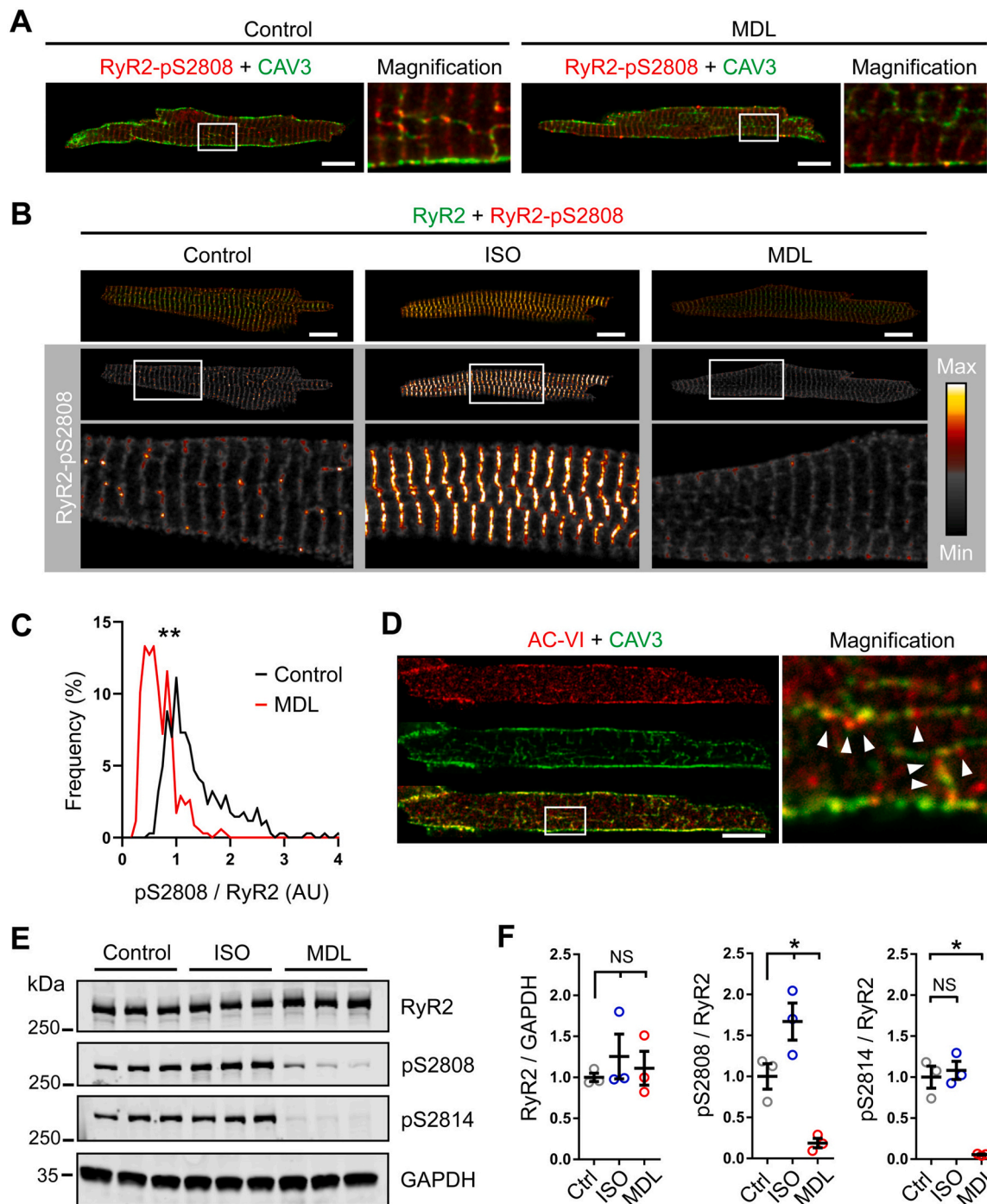


Fig. 5. Adenylyl cyclase inhibition impedes junctional RyR2 cluster phosphorylation. (A) Confocal co-immunostaining of PKA-phosphorylated RyR2-pS2808 and caveolin-3 (CAV3) clusters in AMs under baseline control conditions versus 30 min MDL treatment (100 μ M). *Magnified panels:* The deep intracellular highly phosphorylated RyR2-cluster signals are diminished following MDL treatment at axial tubules identified by CAV3 staining. (B) Co-immunostaining of the RyR2 substrate and RyR2-pS2808 in AMs. Magnified panels comparing the colour-coded RyR2-pS2808 signal intensity changes following 2 min isoproterenol stimulation (100 nM, *middle*) versus 30 min MDL treatment (100 μ M, *right*). (C) Histogram showing the bimodal frequency distribution of the substrate-normalized pS2808/RyR2 cluster signals in untreated control AM (*black trace*): the major peak indicates abundant low or not phosphorylated versus the rightward shoulder few highly phosphorylated RyR2-pS2808 clusters. MDL treatment significantly shifted the phosphorylated pS2808/RyR2 frequency distribution leftward into a major peak of low or not phosphorylated clusters (*red trace*). Histogram data correspond with the exemplary AMs in A and B representative of at least three cell isolations from individual mouse hearts; control 342 RyR2 clusters, MDL 346 RyR2 clusters. $^{**}p < 0.01$, Mann-Whitney *U* test. (D) Confocal AM co-immunostaining of the transmembrane adenylyl cyclase VI (AC-VI) and caveolin-3 (CAV3). Arrowheads identified cluster signals of adenylyl cyclase VI at caveolin-3 positive TAT membrane structures. Immunostaining images in A, B and D are representative of at least three cell isolations from individual mouse hearts. Scale bars 10 μ m. White boxes indicate magnified image regions. (E) Immunoblotting of RyR2, RyR2-pS2808 and CaMKII-phosphorylated RyR2-Ser2814 comparing atrial tissue lysates from WT mouse hearts perfused with control versus isoproterenol (100 nM, 2 min) or MDL (100 μ M, 30 min). (F) Dot plots summarizing phosphorylation changes following isoproterenol versus MDL treatment. $n = 3$ mouse hearts each; immunoblots are representative of three technical replicates. NS, not significant; $^{*}p < 0.05$, unpaired Student's *t*-test. (For interpretation of the references to colour in this figure legend, the reader is referred to the web version of this article.)

diminished the constitutively increased RyR2-pS2808 cluster signals mediated by PKA phosphorylation in AMs (Fig. 5B, MDL).

To quantify the MDL-dependent changes in RyR2 cluster phosphorylation in situ, we analyzed the frequency distribution of the substrate-normalized pS2808/RyR2 cluster signal ratio. Untreated control AMs showed a bimodal frequency distribution with a major leftward peak of the highly abundant low or not Ser2808 phosphorylated non-junctional RyR2 clusters versus a right-skewed shoulder of less abundant but highly phosphorylated junctional RyR2 cluster signals (Fig. 5C, control). Only 2 min of isoproterenol (100 nM) stimulation were sufficient to transform the entire less or not Ser2808 phosphorylated RyR2 cluster population into maximally PKA phosphorylated RyR2 clusters, confirming the efficacy of the β -adrenergic stimulation for living AMs (Supplementary Fig. 15A). In line with previous findings [1], β -adrenergic stimulation shifted the major pS2808/RyR2 cluster frequency not only rightward, but generated a singular frequency peak representing the highly phosphorylated cluster signals (Supplementary Fig. 15B). In contrast, adenylyl cyclase inhibition by MDL significantly shifted the major frequency peak of the less phosphorylated pS2808/RyR2 cluster signals further leftward, whereas the right-skewed frequency distribution was completely diminished consistent with a strongly decreased in situ RyR2 cluster Ser2808 phosphorylation in AMs (Fig. 5C, MDL). Since the MDL treatment shifted the pS2808/RyR2 frequency distribution leftward as compared to the peak of the less phosphorylated untreated baseline cluster population, the major population of non-junctional RyR2 clusters apparently exhibited a low level of Ser2808 phosphorylation of the tetrameric channel in situ (Fig. 5C, MDL).

As the local cAMP-dependent modification through junctional RyR2 cluster phosphorylation may depend on the isoform-specific subcellular distribution of the adenylyl cyclase VI (AC-VI), which was previously characterized in VMs [23], we applied immunostaining and confocal imaging to localize the AC-VI cluster signals in AMs. Indeed, bright signals of AC-VI clusters alternating with caveolin-3 signals confirmed the localization at axial tubules in AMs (Fig. 5D).

Finally, immunoblotting of atrial tissue lysates characterized the RyR2 phosphorylation changes following ex vivo Langendorff treatment of intact mouse hearts: whereas 2 min isoproterenol (100 nM) perfusion significantly increased RyR2 phosphorylation at Ser2808 in atrial tissue lysates, the Ser2814 phosphorylation at the CaMKII-specific phosphosite was not changed (Fig. 5E). In contrast, mouse hearts perfused for 30 min with MDL (100 μ M) showed a strongly diminished Ser2808 phosphorylation in atrial lysates, but additionally a profoundly decreased Ser2814 phosphorylation as compared to the baseline control (Fig. 5E). While isoproterenol stimulation significantly increased the substrate-normalized pS2808/RyR2 but not the pS2814/RyR2 ratio, MDL significantly decreased both the pS2808/RyR2 and the pS2814/RyR2 ratio (Fig. 5F). However, both isoform-specific adenylyl cyclase inhibitors NKY80 and SQ22,536 neither affected the constitutive Ser2808 phosphorylation nor the atrial pS2808/RyR2 ratio (Supplementary Fig. 16). Taken together, these results additionally support a constitutively increased local AC-VI activity at the atrial cell and tissue level, sustaining the compartmentalized junctional RyR2-Ser2808 cluster phosphorylation at baseline. Interestingly, the MDL treatment uncovered a constitutively increased RyR2-Ser2814 phosphorylation, confirming an increased junctional CaMKII activity in AMs reported previously [1].

4.6. Adenylyl cyclase inhibition impairs SR Ca^{2+} release at axial tubule junctions

To assess the functional consequences of the MDL-inhibited junctional adenylyl cyclase activity in AMs, we used confocal transversal line scanning perpendicular to the main cell axis to record field-paced (1 Hz) steady-state Ca^{2+} transients (CaTs). To capture the Ca^{2+} release locally at axial tubules, intracellular Ca^{2+} -imaging with the indicator Fluo-4 was combined with membrane labelling by Chol-PEG-KK114 (Fig. 6A). Apparently, MDL diminished the intensity of the Ca^{2+} release signals at

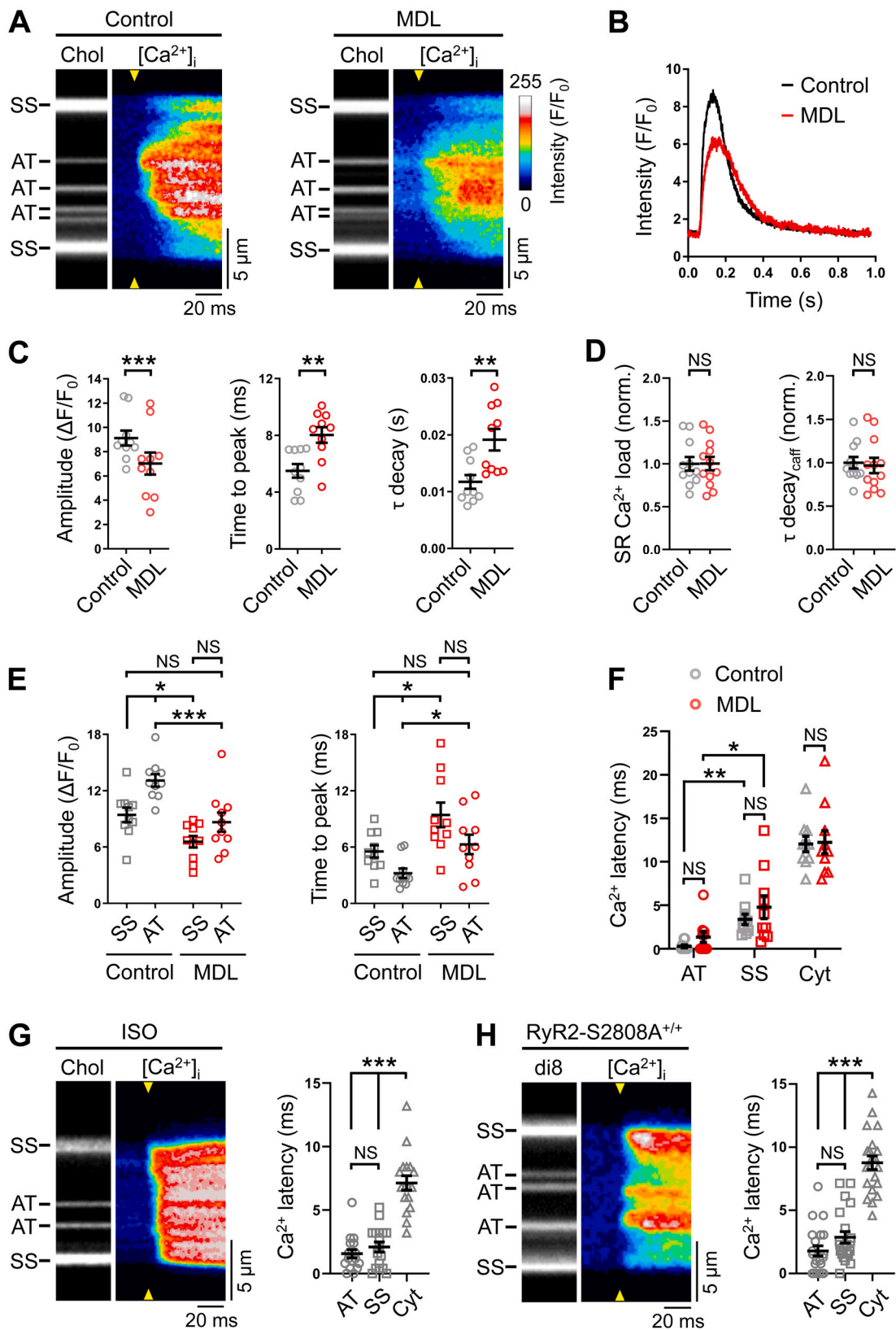
axial tubules resulting in a decreased CaT amplitude (Fig. 6A-B). While MDL significantly decreased the CaT amplitude, the CaT time-to-peak and decay rate were both significantly increased (Fig. 6B and C), consistent with depressed and delayed SR Ca^{2+} release and uptake cycling. Additionally, pairwise comparison of the diastolic Fluo-4 intensity in field-paced AMs indicated a small, but significantly increased diastolic Ca^{2+} concentration following MDL treatment (Supplementary Fig. 17A). In contrast, the caffeine-estimated SR Ca^{2+} load and the caffeine-augmented CaT decay rate were not significantly changed after MDL treatment (Fig. 6D). Taken together, these data suggest that adenylyl cyclase inhibition by MDL diminishes and delays junctional SR Ca^{2+} release through decreased dyadic RyR2 cluster phosphorylation at Ser2808 and Ser2814.

Based on the thorough Chol-PEG-KK114 membrane staining, we next analyzed the local Ca^{2+} release changes at the peripheral subsurface versus axial tubule Ca^{2+} release sites (Supplementary Methods, Combined axial tubule and Ca^{2+} imaging). Under untreated baseline conditions the CaT amplitude and time-to-peak were significantly higher and shorter, respectively, at axial tubule junctions as compared to subsurface sites (Fig. 6E). Adenylyl cyclase inhibition by MDL depressed the CaT amplitude significantly and delayed the CaT time-to-peak both at axial tubule and subsurface Ca^{2+} release sites (Fig. 6E). Furthermore, subcellular latency profiling of the maximal Ca^{2+} signal upstroke velocity (dF/dt_{max}) excluded significant local differences after MDL treatment at axial tubule and subsurface membrane structures as compared to the membrane-free cytosol (Fig. 6F). The latter additionally confirmed the expected temporal latency rank order for the three major classes of subcellular Ca^{2+} release sites in AMs: axial tubules < subsurface sites << membrane-free cytosolic regions [1]. Notably, optical sections (nominal confocal image plane width $\sim 0.8 \mu\text{m}$) of specific AM regions devoid of TAT endomembrane structures occasionally showed U-shaped systolic CaTs as described previously [6–8], but were only rarely observed here (Supplementary Fig. 17B). In summary, MDL treatment uncovered a constitutively augmented cAMP synthesis in junctional compartments mainly at axial tubules, where adenylyl cyclase inhibition particularly blunted the more rapid process of local SR Ca^{2+} release in AMs, molecularly sustained through highly phosphorylated junctional RyR2 clusters at baseline under untreated conditions.

In sharp contrast to MDL treatment, acute isoproterenol stimulation accelerated and increased both the local Ca^{2+} release at subsurface sites and particularly the membrane-free cytosolic sites (Fig. 6G, left). Subcellular latency profiling revealed that isoproterenol stimulation abolished the local 2–3 ms latency difference (baseline) between axial tubule and subsurface Ca^{2+} release sites, while Ca^{2+} release at membrane-free cytosolic sites was accelerated by ~ 7 ms (Fig. 6G, right), further consistent with increased non-junctional RyR2 cluster phosphorylation throughout the cell. To further analyze whether the early Ca^{2+} release at axial tubule junctions under baseline conditions requires local RyR2 cluster phosphorylation, we studied AMs isolated from PKA phosphorylation incompetent RyR2-S2808A^{+/+} knockin mouse hearts. Importantly, RyR2-S2808A^{+/+} AMs showed no significant difference in local Ca^{2+} release onset at axial tubule versus subsurface sites (Fig. 6H). Hence, PKA phosphorylation of RyR2 clusters at axial tubule junctions increased by a constitutively high adenylyl cyclase activity may provide the molecular basis for the rapid physiological Ca^{2+} release inside AMs that activates cellular contraction, whereas β -adrenergic stimulation recruits the great majority of non-junctional RyR2 clusters, accelerating and physiologically increasing Ca^{2+} release for instance during the fight-or-flight response.

4.7. Junctional cAMP compartments maintain the atrial action potential morphology

In addition to RyR2, constitutively increased junctional cAMP levels may modulate voltage-gated ion channels in AMs. Hence, we hypothesized that the atria-specific morphology of the action potential at



(caption on next page)

baseline depends on the increased adenylyl cyclase activity in Ca^{2+} release units. Firstly, we used a non-invasive high-resolution optical approach to directly record action potentials locally at surface membrane versus TAT network component sites. Indeed, random access

multi-photon microscopy (RAMP) imaging of field-paced (0.34 Hz) AMs based on the voltage-sensitive membrane dye di-4-ANE(*F*)PTEA [24] resolved local action potential events at surface membrane and TAT component sites in nominally Ca^{2+} free extracellular buffer solution

Fig. 6. Adenylyl cyclase inhibition diminishes Ca^{2+} release at axial tubules. (A) Combined confocal live imaging of axial tubules (Chol-PEG-KK114, Chol, 1 μM) and intracellular Ca^{2+} release (Fluo-4 AM, 10 μM) in an exemplary mouse AM during 1 Hz field pacing (yellow triangles) prior to (left) and 6 min after MDL treatment (10 μM , right). Transverse line scanning confirmed that the transient Ca^{2+} release occurred earlier at axial tubule (AT) membranes than subsurface (SS) sites, finally followed by the membrane-free cytosolic regions. Additionally, MDL treatment markedly decreased the apparent peaks of the maximal Ca^{2+} signal intensity locally. (B) Comparison of the paired cell-wide intensity showing the inhibitory MDL effects on the Ca^{2+} transient corresponding to A. (C) Dot plots confirming each a significantly decreased mean Ca^{2+} transient amplitude, increased time-to-peak and delayed decay constant τ after MDL treatment (10 μM , 6 min). (D) Dot plots excluding side effects of MDL treatment each on SR Ca^{2+} load and transmembrane $\text{Na}^+/\text{Ca}^{2+}$ -exchange (τ decay_{caff}) estimated during caffeine-induced Ca^{2+} release. (E) Subcellular Ca^{2+} release analysis at subsurface (SS) versus axial tubule (AT) sites under baseline control versus acute MDL treatment (10 μM , 6 min). (F) Spatial latency analysis of the early Ca^{2+} signal upstroke at 25% signal amplitude (dF/dt) at SS, AT and TAT-free cytosolic locations (Cyt) prior to (control) and 6 min after MDL treatment (10 μM , 6 min). (G) Intracellular Ca^{2+} transient during 1 Hz field pacing and spatial latency analysis of AMs acutely stimulated with ISO (100 nm, 90 s), and (H) AMs isolated from RyR2-S2808A^{+/+} mouse hearts. In H, the membrane dye di-8-ANEPPS (di8, 40 μM) was used for membrane imaging. Data points indicate individual cells: $n = 10$ AMs from 3 mouse hearts in C, E and F, paired data; $n = 11$ control / 12 MDL treated AMs from 4 mouse hearts in D, unpaired data; $n = 17$ AMs from 3 mouse hearts in G, and $n = 21$ AMs from 3 RyR2-S2808A^{+/+} hearts in H, paired data. NS, not significant; * $p < 0.05$, ** $p < 0.01$, *** $p < 0.001$, Student's t -test. (For interpretation of the references to colour in this figure legend, the reader is referred to the web version of this article.)

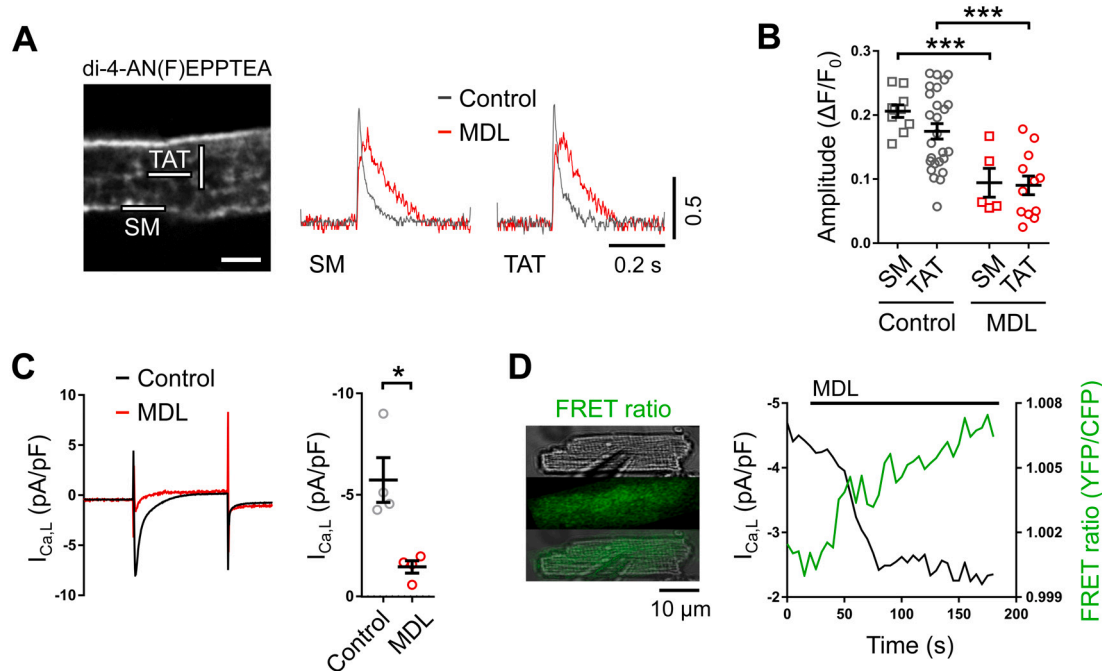


Fig. 7. A constitutively increased adenylyl cyclase activity in junctional compartments regulates action potential morphology and L-type Ca^{2+} current density ($I_{\text{Ca,L}}$) in AMs. (A) Left: 2-photon RAMP action potential imaging with di-4-ANE(F)PTEA (2 μM). White rectangles indicate regions-of-interest used for subcellular voltage-signal recording at transverse (vertical) and axial (horizontal) tubule structures (TAT) versus surface membrane (SM) sites. Scale 5 μm . Right: Corresponding F/F_0 normalized action potential traces each at the SM and TAT structures comparing the baseline control versus acute inhibitory MDL treatment changes (10 μM , 3 min). (B) Dot plot summarizing the significant decreases of the mean amplitude of the action potential both at SM and TAT locations after MDL treatment. $n = 10$ SM versus 26 TAT recordings in 10 AMs under control conditions, and 5 SM versus 12 TAT measurements in 5 AMs following MDL treatment from 3 mouse hearts. *** $p < 0.001$, Student's t -test. (C) Left: Exemplary $I_{\text{Ca,L}}$ current traces from a voltage-clamped AM during depolarization and repolarization of the membrane potential at a rate of 0.5 Hz. Paired $I_{\text{Ca,L}}$ recording comparing the current traces at baseline control versus 2 min after acute MDL treatment (10 μM). Right: Dot plot confirming the strong inhibitory acute MDL effect through a significantly decreased peak $I_{\text{Ca,L}}$ density. $n = 4$ cells from 2 mouse hearts. * $p < 0.05$, Student's t -test. (D) Combined Epac1-JNC transgenic AM voltage-clamping and epifluorescence FRET cAMP imaging during acute adenylyl cyclase inhibition by MDL (10 μM). Left: Snapshot of the AM showing the integrity of the patch-clamped AM structure and pipette position, the FRET ratio YFP/CFP, and the combined imaging data. Right: Time course of $I_{\text{Ca,L}}$ density (black) and reciprocal FRET ratio (green) upon MDL superfusion. Data traces are representative of three cell isolations from individual mouse hearts. (For interpretation of the references to colour in this figure legend, the reader is referred to the web version of this article.)

(Fig. 7A, left; Methods section). Exemplary action potentials recorded simultaneously showed similar morphologies at surface versus TAT membrane sites in AMs (Fig. 7A, black traces). However, acute adenylyl cyclase inhibition by MDL (10 μM) for 3 min apparently blunted the depolarization phase of the action potential, while the repolarization phase was prolonged both at the surface and TAT membrane sites (Fig. 7A, red traces). On average, the MDL treatment of AMs decreased the action potential amplitude significantly (Fig. 7B), while the time-to-peak and action potential repolarization (APD_{50}) were markedly prolonged both at the surface and TAT membrane sites (Supplementary Fig. 18A–B). While the precise molecular mechanisms of the local MDL-induced action potential prolongation are beyond the scope of this

study, we note that the MDL-treated AMs showed more variable changes of the time-to-peak and the APD_{50} values (Supplementary Fig. 18), whereas the amplitude decrease was tightly clustered (Fig. 7B). The latter observation confirmed the pronounced effect of acute adenylyl cyclase inhibition by MDL on the depolarization phase of the atrial action potential.

Secondly, the molecular mechanism of the cAMP-dependent PKA regulation of both the $\text{Ca}_v1.2$ and $\text{Ca}_v1.3$ LTCC channel isoforms has been identified only recently: at baseline, the small G-protein Rad directly inhibits the cardiac LTCC activity through binding to its β -subunit, while PKA phosphorylation of Rad causes it to leave the vicinity of the macromolecular channel complex, resulting in PKA-

mediated activation of the LTCC channel [25–27]. Hence, we hypothesized that the constitutively increased junctional cAMP levels additionally sustain an increased activity of the atrial LTCC Ca^{2+} currents at baseline in untreated AMs. Interestingly, both pore-forming subunit isoforms, the ubiquitous cardiac $\text{Ca}_v1.2\text{-}\alpha1\text{C}$ and the atria-specific $\text{Ca}_v1.3\text{-}\alpha1\text{C}$, were demonstrated with high cluster densities in the axial tubule components of mouse AMs recently [1,2]. Using whole-cell patch-clamp, we confirmed robust LTCC currents ($I_{\text{Ca,L}}$) in mouse AMs depolarized at 0.5 Hz, generating a high peak $I_{\text{Ca,L}}$ density at baseline (Fig. 7C, *control*). Strikingly, acute MDL treatment (10 μM) for 2 min strongly decreased the peak $I_{\text{Ca,L}}$ density (Fig. 7C, *MDL*), confirming earlier observations in patch-clamped guinea pig AMs reported previously [28]. **Supplementary Fig. 19** illustrates the gradual decrease of the $I_{\text{Ca,L}}$ density after acute MDL treatment over time, which occurred markedly earlier compared to the spontaneous run-down of the $I_{\text{Ca,L}}$ density.

Finally, to characterize the temporal relationship between the junctional cAMP decrease following MDL treatment and the diminished $I_{\text{Ca,L}}$ density, we performed simultaneous epifluorescence FRET cAMP and patch-clamp measurements in Epac1-JNC transgenic AMs. While the FRET ratio showed an initially rapid followed by a slower increase during 3 min recording, the peak $I_{\text{Ca,L}}$ density was submaximally decreased within ~ 1 min (Fig. 7D). Hence, acute MDL treatment decreased both the junctional cAMP levels and the $I_{\text{Ca,L}}$ density rapidly in AMs. While this acute inhibitory MDL effect identified a major role of the constitutively increased adenylyl cyclase activity for the augmented LTCC channel function in AMs, at baseline both the cell type-specific action potential morphology and the rapid atrial CICR activation depended molecularly on the sustained cAMP synthesis in the Ca^{2+} release units.

5. Discussion

In the present study we showed that junctin, a SR membrane-anchored and RyR2-binding protein [29], is predominantly localized in the junctional Ca^{2+} release units of AMs. In contrast, the great majority of non-junctional RyR2 clusters did not exhibit any similarly apparent signal co-localization with the junctin clusters. Based on this AM-specific junctin cluster distribution mainly in axial tubule junctions, we established a junction-specific cAMP FRET imaging approach employing a novel Epac1-JNC biosensor transgenically expressed in cardiomyocytes of a recently established mouse model [13]. Strikingly, similar to the subcellular distribution of endogenous junctin, the Epac1-JNC biosensor was localized exclusively in junctional clusters, confirming a central prerequisite to monitor cAMP levels specifically in the dyadic cleft of living AMs. While co-immunoprecipitation further established an interaction between the endogenous RyR2 and junctin proteins, the transgenic Epac1-JNC was confirmed as an exogenous RyR2 interactor. High-resolution confocal FRET imaging demonstrated constitutively augmented cAMP levels at axial tubule junctions, where the major physiological sites for baseline junctional Ca^{2+} release are located in AMs. Interestingly, the constitutively augmented cAMP levels at axial tubule junctions maintain *both* the increased junction-specific RyR2 cluster PKA phosphorylation and increased $I_{\text{Ca,L}}$ currents, underpinning the rapid and high-gain activation of CICR at baseline in AMs. As each $\text{Ca}_v1.2$ and $\text{Ca}_v1.3$, as well as RyR2 exist highly clustered in atrial Ca^{2+} release units [1,2], we propose that the constitutively increased junctional cAMP levels prime CICR at axial tubule junctions through molecularly synergistic and sustained posttranslational modifications at baseline. Consistent with this model, inhibition of the sustained cAMP-generating activity by pharmacological pan-inhibition of the cardiac adenylyl cyclase isoforms greatly diminished the $I_{\text{Ca,L}}$ current density and the junctional RyR2 phosphorylation, leading to both a significantly decreased and delayed Ca^{2+} release at axial tubule sites in AMs.

Unexpectedly, we found that junctin is differentially distributed in

AMs but not in VMs. Within the quaternary Ca^{2+} release macromolecular complex, junctin is supposed to function as interaction partner each of RyR2, triadin, and calsequestrin-2 in the SR membrane and lumen [10,30]. Whereas RyR2 stably interacts with junctin, calsequestrin-2 was shown to dissociate from junctin at increased Ca^{2+} levels with an IC_{50} of 0.6–0.8 mM [10,30]. Moreover, both junctin knockdown in rat VMs by antisense RNA or germ-line junctin knockout in mice increased SR Ca^{2+} load, Ca^{2+} release, and contractility [12,31]. Interestingly, while the junctin knockout did not affect the heart structurally, 25% of the junctin knockout mice died by three months age spontaneously, while isoproterenol stimulation induced fatal arrhythmias [12]. Vice versa, cardiomyocyte-restricted junctin overexpression in mice decreased both the SR Ca^{2+} load and Ca^{2+} spark frequency in VMs, leading to a decreased contractility and cardiac hypertrophy [32,33]. In sharp contrast, while we established a 5-fold lower junctin expression level in the atria compared to the ventricles in paired samples from the same hearts (Fig. 1A), rodent AMs exhibit a 2-fold higher SR Ca^{2+} load and mouse atria a 3-fold higher SERCA2a protein expression [1,34].

The exclusive clustering of atrial junctin in junctional Ca^{2+} release sites (Figs. 1B and E) broadens the concept that RyR2 clusters are differentially regulated in AMs as proposed previously [1,3]. At junctional Ca^{2+} release sites in AMs we confirmed that RyR2 clusters were highly phosphorylated by PKA and CaMKII [1]. Vice versa, little or no junctin co-localization was evidenced for the great majority of non-junctional atrial RyR2 clusters. Non-junctional RyR2 channels are thus expected to bind less or no calsequestrin-2 and may experience a fundamentally different local SR luminal Ca^{2+} environment [11,35]. Importantly, the calsequestrin-2 protein level in atrial compared to ventricular tissue was $31 \pm 0.05\%$ lower (Fig. 1A), suggesting that the observed junctin clustering may additionally contribute to the local and Ca^{2+} concentration-dependent calsequestrin-2 accumulation at the luminal side of junctional RyR2 clusters. A previous study was not conclusive, since only a non-significant trend indicated a potentially lower atrial calsequestrin-2 expression level in rat cardiac lysates based on the same antibody used here for immunoblotting [34]. Interestingly, consistent with abundant junctional junctin clustering, junctional but not non-junctional Ca^{2+} release sites generate significantly larger Ca^{2+} mega-sparks at axial tubules in mouse AMs, as confirmed conceptually by mathematical modeling [1].

Furthermore, the membrane tethering protein junctophilin-2 shows the same subcellular distribution pattern and preferential junctional clustering as junctin in AMs [3]. Whereas junctophilin-2 binds negatively charged phospholipids in the sarcolemma, junctin exhibits a significantly shorter 22 amino acid long cytoplasmic N-terminus, which cannot physically bridge the dyadic cleft subspace [36]. While junctophilin-2 was established as an essential protein for the junctional membrane organization both in AMs and VMs [3,37,38], the precise molecular roles of junctin for junctional RyR2 clustering and luminal regulation by calsequestrin-2 in AMs need to be addressed by future studies. As TAT membrane components are reorganized and RyR2 channels might become non-junctional (“RyR2 orphaning”) during heart disease [1,14], [39] the latter may also affect the junctin clustering. Interestingly, on top of the significantly lower atrial junctin levels at baseline, we observed a 52% decrease in junctin expression four weeks after transaortic constriction in mouse left atria (data not shown) in line with the significantly decreased left-ventricular junctin levels in human failing hearts reported previously [40].

While the here reported atria-specific subcellular cAMP signaling and compartmentation mechanisms answer open cell biology questions, we additionally propose an emerging fundamental role for axial tubule junctions as the major cell type-specific Ca^{2+} release mechanism, significantly extending earlier studies [1,2]. Notably, while cAMP biosensors targeted by fusion proteins to specific subcellular compartments were mainly applied in VMs [41–43], we developed a state-of-the-art confocal FRET approach to detect subcellular cAMP levels locally for the first time in living AMs. A combination of FRET epifluorescence

imaging and scanning ion conductance microscopy (SICM) at the surface of VMs spatially resolved cAMP microdomains at the crest versus T-tubule orifice as reported previously [44]. However, the utility of combined epifluorescence and SICM imaging for AMs appears limited, as the major functionally relevant cAMP compartments at axial tubule junctions are not captured by this technique. Furthermore, isolated AMs are exquisitely sensitive to experimental phototoxic and mechanical noxae, and the latter can directly disrupt the tubular membrane structures as demonstrated by STED imaging in AMs [2]. For these reasons, we pioneered a confocal live-cell FRET imaging approach to improve the intracellular spatial resolution for non-invasive all optical AM studies. Combined with a previously established customized membrane labelling protocol for living AMs [2], this enabled us to monitor the local cAMP concentrations in junctional compartments despite the relatively low Epac1-JCN expression level. Thus, based on the exclusive Epac1-JCN colocalization with junctional RyR2 clusters, the baseline and pharmacologically altered cAMP levels were directly captured in the junctional compartments at axial tubules and the surface membrane. Interestingly, while we confirmed each the highly phosphorylated junctional versus low or not phosphorylated non-junctional RyR2 clusters as distinct channel populations, the cardiac AC-VI isoform was frequently clustered at the TAT membrane structures in AMs (Fig. 5). Taken together, this supports a new concept of locally sustained cAMP compartmentation at baseline in AM junctions, whereas acute β -adrenergic stimulation leads to increased cAMP synthesis at the junctional Ca^{2+} release sites and globally increased RyR2-Ser2808 phosphorylation within minutes throughout the cell (Fig. 5B and Supplementary Fig. 15). This is in line with a previous report of cell-wide restored CICR in detubulated rat ventricular myocytes through β -adrenergic stimulation [45].

Earlier studies have focused on the specific roles of cAMP hydrolyzing phosphodiesterase subfamilies (PDE1, PDE2, PDE3 and PDE4) in rodent and human myocardium [46,47]. Whereas both in AMs and VMs the PDE4 subfamily isoforms control cAMP locally and directly in the RyR2 macromolecular channel complex, this confined cAMP hydrolysis becomes significantly impaired in atrial fibrillation and heart failure due to depressed PDE4D expression and diminished RyR2 interactions [9,13,47]. Both PKA and PDE4D3 bind to mAKAP (A-kinase anchoring protein AKAP6), contributing to a ternary complex that interacts with and directly regulates RyR2 channel activity [48]. Vice versa, PDE4D3 itself is dynamically regulated by a negative feedback loop, which affects RyR2 phosphorylation both at baseline and increased β -adrenergic stimulation [49]. Since junctional RyR2 clusters in AMs exhibit a constitutively increased RyR2 phosphorylation, AMs are characterized by a cell-specific cAMP-dependent compartmental mechanism quite different from VMs. Based on the increased junctional PKA phosphorylation of RyR2 channels both at Ser2808 and Ser2814 at baseline without any exogenous β -adrenergic stimulation, we propose a direct functional role for a constitutively increased adenylyl cyclase activity in combination with PDE4D3-dependent regulation in AMs [1]. Indeed, MDL inhibition unmasked the increased adenylyl cyclase activity at the subcellular Ca^{2+} release sites of axial tubule junctions, directly supporting the concept that increased junctional cAMP levels sustain the increased junctional RyR2-Ser2808 cluster phosphorylation, underlying both the rapid and augmented atrial SR Ca^{2+} release in the dyadic cleft. Future studies may thus elucidate the precise subcellular organization and role of phosphodiesterases in the junctional compartments of AMs.

Adenylyl cyclase enzymes have been previously localized by metal precipitation labelling and electron microscopy immunolabelling in the surface sarcolemma and in transverse tubules of adult guinea pig VMs [50]. Moreover, the adenylyl cyclases V/VI (AC-V/VI) were established as the predominant isoforms expressed in the ventricles and in VMs [4,23,51], actually with similar expression levels in the atrial versus ventricular mouse tissues [1]. While the non-selective adenylyl cyclase inhibitor MDL efficiently decreased the junctional cAMP generation in AMs, the selective AC-V inhibitor NKY80 did not affect the dyadic cAMP level in AMs (Supplementary Figs. 14) [21,52,53]. Similarly, the

junctional cAMP level in AMs treated with the AC-V selective inhibitor SQ22,536 was not changed [21,52,53]. However, the selective pharmacological targeting of AC-V by NKY80 and SQ22,536 has been challenged recently [54,55]. Immunostaining and confocal imaging showed AC-VI clusters for the first time at TAT membrane structures in AMs (Fig. 5D). Notably, the Ca^{2+} -sensitive AC-I and AC-VIII isoforms were previously localized mainly in the cortical region at the surface sarcolemma of AMs [28,56], indicating principally different subcellular adenylyl cyclase localizations. Together with the constitutively increased LTCC currents and RyR2 Ca^{2+} release in AMs, this may at least partly explain the constitutively increased AC-VI isoform-specific activity in the junctional compartments in AMs. Nonetheless, future studies will have to establish the differential adenylyl cyclase isoform expression and localization at axial tubule junctions versus other locations, and if the AC-VI isoform is molecularly essential for the sustained dyadic baseline cAMP synthesis, underpinning the atrial action potential and augmenting CICR constitutively for rapid contractile activation locally at baseline in AMs.

The proposed mechanism of AC-dependent subcellular cAMP pools significantly extends the previous putative model of physiological CICR in AMs [1], but may also reveal a particular vulnerability of AMs for pathological membrane remodeling and altered intracellular Ca^{2+} signaling. Axial tubule reorganization with a decrease of dyadic junctions in atrial disease implies a loss-of-function at the CICR level [1,3], perhaps explaining the susceptibility for highly prevalent supraventricular arrhythmias like atrial fibrillation and worsening of heart failure in the aging heart. Moreover, β -adrenergic stimulation effectively accelerates and amplifies Ca^{2+} release in AMs through recruitment of the great majority of non-junctional RyR2 clusters, which may however disturb local atrial CICR control during heart disease-sustained catecholaminergic stress in heart failure patients. This may further explain at least partly the benefit of β -blocker therapy in atrial fibrillation patients with and without concomitant heart failure [57]. The present study may help to identify early atria-specific disease mechanisms that underlie the recent concept of atrial cardiomyopathies [58], which may ultimately facilitate the development of new and atria-specific therapeutic strategies.

5.1. Study limitations

In contrast to some previous models based on isolated AMs devoid of any TAT structures [6], we have confirmed cell-wide TAT networks in 100% of isolated adult mouse AMs based on an isolation and staining protocol optimized for high-resolution live-cell imaging (Supplementary Fig. 10). Here, AMs were jointly isolated both from the left and right atria to gain sufficiently high numbers of high-quality cells for functional cAMP, Ca^{2+} and structural TAT imaging analyses. Nonetheless, future studies need to compare differences between left and right AMs to address the chamber-specific TAT network architecture.

Confocal Ca^{2+} imaging in AMs confirmed a relatively small but significant latency difference of the early subcellular Ca^{2+} signal onset ranked in the order axial tubules < subsurface sites << TAT-free cytosolic regions [1], a hierarchy however not significantly changed by acute adenylyl cyclase inhibition (Fig. 6F). In contrast, ablating junctional RyR2 phosphorylation by PKA in RyR2-Ser2808Ala knockin mice diminished the latency difference between axial tubule versus subsurface Ca^{2+} release onset in AMs (Fig. 6H). Notably, the confocal transverse line-scanning applied here technically cannot fully capture, and, thus, underestimates sparse transverse tubule structures in AMs due to their complex 3D spatial meandering orientations during live-cell imaging. While axial tubules are reliably identified due to their relative large diameter, the AM-specific subcellular Ca^{2+} signal behaviors represent a complex 3D spatiotemporal diffusion process [1,59], however, at diffraction-limited confocal resolution. Future studies will need to develop, verify, and extend these spatially limited but conceptually important aspects to quantitatively study the subcellular CICR

mechanisms at higher spatiotemporal resolution in AMs based on advanced live-cell superresolution 2D and 3D Ca^{2+} imaging and mathematical modeling techniques.

Funding

This work was supported by Deutsche Forschungsgemeinschaft to SB (SFB1002 project A09), SEL (SFB1002 projects A09 and S02; SFB1190 project P03), GH (SFB1002 project D01), NV (SFB1002 project A13, VO 1568/3–1, VO 1568/4–1, IRTG1816), VON (SFB1002 project A01); and under Germany's Excellence Strategy - EXC 2067/1–390729940. VON was supported by the Gertraud und Heinz Rose-Foundation. NV received funding from the Else-Kröner-Fresenius Foundation (EKFS 2016_A20). JP was supported by the German Cardiac Society (Otto-Hess-Scholarship). SB received financial support through a DZHK (German Centre for Cardiovascular Research) postdoc start-up grant (81X3300108), and the clinician scientist program “Translational Medicine” of the University Medical Center Göttingen. GH, NV, SEL, VON are principal investigators of the DZHK (German Centre for Cardiovascular Research).

Author contributions

SB, JP and SEL designed the studies. DU, HS, JP, JW, LS, MM, MS, NV, SB, SEL, SIA, TK, VON and VS performed the research and analyzed the data. DA and DS provided the junctin knockout animals. SB, JP and SEL wrote the manuscript, and all authors contributed to the final version.

Disclosures

The authors have declared no conflicts of interest. Competing interests: S.E.L. is an inventor on a patent (US 20070089572A1) submitted by Columbia University “Novel agents for preventing and treating disorders involving modulation of RYR receptors.”

Acknowledgements

We are grateful for excellent technical assistance by Birgit Schumann and Brigitte Korff. We thank Karl Pfeifer for kindly sharing the immunogen information to generate the junctin antibody.

Appendix A. Supplementary data

Supplementary data to this article can be found online at <https://doi.org/10.1016/j.jmcc.2022.01.003>.

References

- Brandenburg, T. Kohl, G.S. Williams, K. Gusev, E. Wagner, E.A. Rog-Zielinska, E. Heibisch, M. Dura, M. Didie, M. Gotthardt, V.O. Nikolaev, G. Hasenfuss, P. Kohl, C.W. Ward, W.J. Lederer, S.E. Lehnart, Axial tubule junctions control rapid calcium signaling in atria, *J. Clin. Invest.* 126 (2016) 3999–4015.
- Brandenburg, J. Pawlowitz, F.E. Fakuade, D. Kownatzki-Danger, T. Kohl, G. Y. Mitronova, M. Scardigli, J. Neef, C. Schmidt, F. Wiedmann, F.S. Pavone, L. Sacconi, I. Kutschka, S. Sossalla, T. Moser, N. Voigt, S.E. Lehnart, Axial tubule junctions activate atrial Ca^{2+} release across species, *Front. Physiol.* 9 (2018) 1227.
- Brandenburg, J. Pawlowitz, B. Eikenbusch, J. Peper, T. Kohl, G.Y. Mitronova, S. Sossalla, G. Hasenfuss, X.H. Wehrens, P. Kohl, E.A. Rog-Zielinska, S.E. Lehnart, Junctophilin-2 expression rescues atrial dysfunction through polyadic junctional membrane complex biogenesis, *JCI Insight.* 4 (2019).
- A.M. Feldman, Adenylyl cyclase: a new target for heart failure therapeutics, *Circulation.* 105 (2002) 1876–1878.
- T.J. Hund, P.J. Mohler, Atrial-specific pathways for control of intracellular signaling and myocyte function, *J. Clin. Invest.* 126 (2016) 3731–3734.
- M.D. Bootman, D.R. Higazi, S. Coombes, H.L. Roderick, Calcium signalling during excitation-contraction coupling in mammalian atrial myocytes, *J. Cell Sci.* 119 (2006) 3915–3925.
- J.R. Berlin, Spatiotemporal changes of Ca^{2+} during electrically evoked contractions in atrial and ventricular cells, *Am. J. Phys.* 269 (1995) H1165–H1170.
- J. Huser, S.L. Lipsius, L.A. Blatter, Calcium gradients during excitation-contraction coupling in cat atrial myocytes, *J. Physiol.* 494 (Pt 3) (1996) 641–651.
- S.E. Lehnart, X.H. Wehrens, S. Reiken, S. Warrier, A.E. Belevych, R.D. Harvey, W. Richter, S.L. Jin, M. Conti, A.R. Marks, Phosphodiesterase 4D deficiency in the ryanodine-receptor complex promotes heart failure and arrhythmias, *Cell.* 123 (2005) 25–35.
- L. Zhang, J. Kelley, G. Schmeisser, Y.M. Kobayashi, L.R. Jones, Complex formation between junctin, triadin, calsequestrin, and the ryanodine receptor. Proteins of the cardiac junctional sarcoplasmic reticulum membrane, *J. Biol. Chem.* 272 (1997) 23389–23397.
- I. Gyorke, N. Hester, L.R. Jones, S. Gyorke, The role of calsequestrin, triadin, and junctin in conferring cardiac ryanodine receptor responsiveness to luminal calcium, *Biophys. J.* 86 (2004) 2121–2128.
- Q. Yuan, G.C. Fan, M. Dong, B. Altschaff, A. Diwan, X. Ren, H.H. Hahn, W. Zhao, J. R. Wagoner, L.R. Jones, W.K. Jones, D.M. Bers, G.W. Dorn 2nd, H.S. Wang, H. H. Valdivia, G. Chu, E.G. Kranias, Sarcoplasmic reticulum calcium overloading in junctin deficiency enhances cardiac contractility but increases ventricular automaticity, *Circulation.* 115 (2007) 300–309.
- F. Berisha, K. Götz, J.W. Wegener, S. Brandenburg, H. Subramanian, C.E. Molina, A. Rueffer, J. Petersen, A. Bernhardt, E. Girdauskas, C. Jungen, U. Pape, A.E. Kraft, S. Warnke, D. Lindner, D. Westermann, S. Blankenberg, C. Meyer, G. Hasenfuss, S. E. Lehnart, V.O. Nikolaev, cAMP imaging at ryanodine receptors reveals beta2-adrenoceptor driven arrhythmias, *Circ. Res.* 129 (2021) 81–94.
- S. Brandenburg, T. Kohl, S.E. Lehnart, Analysis of tubular membrane networks in cardiac myocytes from atria and ventricles, *J. Vis. Exp.* (2014) e51823.
- D. Calebiro, V.O. Nikolaev, M.C. Gagliani, T. de Filippis, C. Dees, C. Tacchetti, L. Persani, M.J. Lohse, Persistent cAMP-signals triggered by internalized G-protein-coupled receptors, *PLoS Biol.* 7 (2009), e1000172.
- S. Borner, F. Schwede, A. Schlipp, F. Berisha, D. Calebiro, M.J. Lohse, V. O. Nikolaev, FRET measurements of intracellular cAMP concentrations and cAMP analog permeability in intact cells, *Nat. Protoc.* 6 (2011) 427–438.
- C. Crocini, C. Ferrantini, M. Scardigli, R. Coppini, L. Mazzoni, E. Lazzeri, J. M. Pioner, B. Scellini, A. Guo, L.S. Song, P. Yan, L.M. Loew, J. Tardiff, C. Tesi, F. Vanzi, E. Cerbai, F.S. Pavone, L. Sacconi, C. Poggesi, Novel insights on the relationship between T-tubular defects and contractile dysfunction in a mouse model of hypertrophic cardiomyopathy, *J. Mol. Cell. Cardiol.* 91 (2016) 42–51.
- M. Scardigli, C. Crocini, C. Ferrantini, T. Gabbriellini, L. Silvestri, R. Coppini, C. Tesi, E.A. Rog-Zielinska, P. Kohl, E. Cerbai, C. Poggesi, F.S. Pavone, L. Sacconi, Quantitative assessment of passive electrical properties of the cardiac T-tubular system by FRAP microscopy, *Proc. Natl. Acad. Sci. U. S. A.* 114 (2017) 5737–5742.
- S. Treves, M. Vukcevic, M. Maj, R. Thurnheer, B. Mosca, F. Zorzato, Minor sarcoplasmic reticulum membrane components that modulate excitation-contraction coupling in striated muscles, *J. Physiol.* 587 (2009) 3071–3079.
- B. Hein, K.I. Willig, S.W. Hell, Stimulated emission depletion (STED) nanoscopy of a fluorescent protein-labeled organelle inside a living cell, *Proc. Natl. Acad. Sci. U. S. A.* 105 (2008) 14271–14276.
- T. Onda, Y. Hashimoto, M. Nagai, H. Kuramochi, S. Saito, H. Yamazaki, Y. Toya, I. Sakai, C.J. Homcy, K. Nishikawa, Y. Ishikawa, Type-specific regulation of adenylyl cyclase. Selective pharmacological stimulation and inhibition of adenylyl cyclase isoforms, *J. Biol. Chem.* 276 (2001) 47785–47793.
- J. Shan, A. Kushnir, M.J. Betzenhauser, S. Reiken, J. Li, S.E. Lehnart, N. Lindegger, M. Mongillo, P.J. Mohler, A.R. Marks, Phosphorylation of the ryanodine receptor mediates the cardiac fight or flight response in mice, *J. Clin. Invest.* 120 (2010) 4388–4398.
- T. Tang, M.H. Gao, N.C. Lai, A.L. Firth, T. Takahashi, T. Guo, J.X. Yuan, D.M. Roth, H.K. Hammond, Adenylyl cyclase type 6 deletion decreases left ventricular function via impaired calcium handling, *Circulation.* 117 (2008) 61–69.
- P. Yan, C.D. Acker, W.L. Zhou, P. Lee, C. Bollensdorff, A. Negrean, J. Lotti, L. Sacconi, S.D. Antic, P. Kohl, H.D. Mansvelder, F.S. Pavone, L.M. Loew, Palette of fluorinated voltage-sensitive hemicyanine dyes, *Proc. Natl. Acad. Sci. U. S. A.* 109 (2012) 20443–20448.
- L. Yang, A. Katchman, J. Kushner, A. Kushnir, S.I. Zakharov, B.X. Chen, Z. Shuja, P. Subramanyam, G. Liu, A. Papa, D. Roybal, G.S. Pitt, H.M. Colecraft, S.O. Marx, Cardiac $\text{Ca}_v1.2$ channels require beta subunits for beta-adrenergic-mediated modulation but not trafficking, *J. Clin. Invest.* 129 (2019) 647–658.
- G. Liu, A. Papa, A.N. Katchman, S.I. Zakharov, D. Roybal, J.A. Hennessey, J. Kushner, L. Yang, B.X. Chen, A. Kushnir, K. Dantas, S.P. Gygi, G.S. Pitt, H. M. Colecraft, M. Ben-Johny, M. Kalocsay, S.O. Marx, Mechanism of adrenergic $\text{Ca}_v1.2$ stimulation revealed by proximity proteomics, *Nature.* 577 (2020) 695–700.
- A. Papa, J. Kushner, J.A. Hennessey, A.N. Katchman, S.I. Zakharov, B.X. Chen, L. Yang, R. Lu, S. Leong, J. Diaz, G. Liu, D. Roybal, X. Liao, P.J. Del Rivero Morfin, H.M. Colecraft, G.S. Pitt, O. Clarke, V. Topkara, M. Ben-Johny, S.O. Marx, Adrenergic $\text{Ca}_v1.2$ activation via rad phosphorylation converges at α_{1C} I-II loop, *Circ. Res.* 128 (2021) 76–88.
- T.P. Collins, D.A. Terrar, Ca^{2+} -stimulated adenylyl cyclases regulate the L-type Ca^{2+} current in guinea-pig atrial myocytes, *J. Physiol.* 590 (2012) 1881–1893.
- T.J. Pritchard, E.G. Kranias, Junctin and the histidine-rich Ca^{2+} binding protein: potential roles in heart failure and arrhythmogenesis, *J. Physiol.* 587 (2009) 3125–3133.
- D.W. Shin, J. Ma, D.H. Kim, The asp-rich region at the carboxyl-terminus of calsequestrin binds to Ca^{2+} and interacts with triadin, *FEBS Lett.* 486 (2000) 178–182.
- G.C. Fan, Q. Yuan, W. Zhao, G. Chu, E.G. Kranias, Junctin is a prominent regulator of contractility in cardiomyocytes, *Biochem. Biophys. Res. Commun.* 352 (2007) 617–622.

- [32] U. Kirchhefer, J. Neumann, D.M. Bers, I.B. Buchwalow, L. Fabritz, G. Hanske, I. Justus, B. Riemann, W. Schmitz, L.R. Jones, Impaired relaxation in transgenic mice overexpressing junctin, *Cardiovasc. Res.* 59 (2003) 369–379.
- [33] U. Kirchhefer, G. Hanske, L.R. Jones, I. Justus, L. Kaestner, P. Lipp, W. Schmitz, J. Neumann, Overexpression of junctin causes adaptive changes in cardiac myocyte Ca^{2+} signaling, *Cell Calcium* 39 (2006) 131–142.
- [34] A.P. Walden, K.M. Dibb, A.W. Trafford, Differences in intracellular calcium homeostasis between atrial and ventricular myocytes, *J. Mol. Cell. Cardiol.* 46 (2009) 463–473.
- [35] J. Qin, G. Valle, A. Nani, A. Nori, N. Rizzi, S.G. Priori, P. Volpe, M. Fill, Luminal Ca^{2+} regulation of single cardiac ryanodine receptors: insights provided by calsequestrin and its mutants, *J. Gen. Physiol.* 131 (2008) 325–334.
- [36] L.R. Jones, L. Zhang, K. Sanborn, A.O. Jorgensen, J. Kelley, Purification, primary structure, and immunological characterization of the 26-kDa calsequestrin binding protein (junctin) from cardiac junctional sarcoplasmic reticulum, *J. Biol. Chem.* 270 (1995) 30787–30796.
- [37] D.L. Beavers, A.P. Landstrom, D.Y. Chiang, X.H. Wehrens, Emerging roles of junctophilin-2 in the heart and implications for cardiac diseases, *Cardiovasc. Res.* 103 (2014) 198–205.
- [38] A. Guo, X. Zhang, V.R. Iyer, B. Chen, C. Zhang, W.J. Kutschke, R.M. Weiss, C. Franzini-Armstrong, L.S. Song, Overexpression of junctophilin-2 does not enhance baseline function but attenuates heart failure development after cardiac stress, *Proc. Natl. Acad. Sci. U. S. A.* 111 (2014) 12240–12245.
- [39] L.S. Song, E.A. Sobie, S. McCulle, W.J. Lederer, C.W. Balke, H. Cheng, Orphaned ryanodine receptors in the failing heart, *Proc. Natl. Acad. Sci. U. S. A.* 103 (2006) 4305–4310.
- [40] U. Gergs, T. Berndt, J. Buskase, L.R. Jones, U. Kirchhefer, F.U. Muller, K. D. Schluter, W. Schmitz, J. Neumann, On the role of junctin in cardiac Ca^{2+} handling, contractility, and heart failure, *Am. J. Physiol. Heart Circ. Physiol.* 293 (2007) H728–H734.
- [41] J.U. Sprenger, R.K. Perera, J.H. Steinbrecher, S.E. Lehnart, L.S. Maier, G. Hasenfuss, V.O. Nikolaev, In vivo model with targeted cAMP biosensor reveals changes in receptor-microdomain communication in cardiac disease, *Nat. Commun.* 6 (2015) 6965.
- [42] Z. Bastug-Ozel, P.T. Wright, A.E. Kraft, D. Pavlovic, J. Howie, A. Froese, W. Fuller, J. Gorelik, M.J. Shattock, V.O. Nikolaev, Heart failure leads to altered beta2-adrenoceptor/cyclic adenosine monophosphate dynamics in the sarcolemmal phospholemman/Na K ATPase microdomain, *Cardiovasc. Res.* 115 (2019) 546–555.
- [43] R.K. Perera, J.U. Sprenger, J.H. Steinbrecher, D. Hubscher, S.E. Lehnart, M. Abesser, K. Schuh, A. El-Armouche, V.O. Nikolaev, Microdomain switch of cGMP-regulated phosphodiesterases leads to ANP-induced augmentation of beta-adrenoceptor-stimulated contractility in early cardiac hypertrophy, *Circ. Res.* 116 (2015) 1304–1311.
- [44] V.O. Nikolaev, A. Moshkov, A.R. Lyon, M. Miragoli, P. Novak, H. Paur, M.J. Lohse, Y.E. Korchev, S.E. Harding, J. Gorelik, Beta2-adrenergic receptor redistribution in heart failure changes cAMP compartmentation, *Science*. 327 (2010) 1653–1657.
- [45] F. Brette, P. Rodriguez, K. Komukai, J. Colyer, C.H. Orchard, beta-adrenergic stimulation restores the Ca^{2+} transient of ventricular myocytes lacking t-tubules, *J. Mol. Cell. Cardiol.* 36 (2004) 265–275.
- [46] F. Rochais, A. Abi-Gerges, K. Horner, F. Lefebvre, D.M. Cooper, M. Conti, R. Fischmeister, G. Vandecasteele, A specific pattern of phosphodiesterases controls the cAMP signals generated by different G_s -coupled receptors in adult rat ventricular myocytes, *Circ. Res.* 98 (2006) 1081–1088.
- [47] C.E. Molina, J. Leroy, W. Richter, M. Xie, C. Scheitrum, I.O. Lee, C. Maack, C. Rucker-Martin, P. Donzeau-Gouge, I. Verde, A. Llach, L. Hove-Madsen, M. Conti, G. Vandecasteele, R. Fischmeister, Cyclic adenosine monophosphate phosphodiesterase type 4 protects against atrial arrhythmias, *J. Am. Coll. Cardiol.* 59 (2012) 2182–2190.
- [48] K.L. Dodge, S. Khouangsathien, M.S. Kamiloff, R. Mouton, E.V. Hill, M.D. Houslay, L.K. Langeberg, J.D. Scott, mA KAP assembles a protein kinase A/PDE4 phosphodiesterase cAMP signaling module, *EMBO J.* 20 (2001) 1921–1930.
- [49] K.L. Dodge-Kafka, J. Soughayer, G.C. Pare, J.J. Carlisle Michel, L.K. Langeberg, M. S. Kamiloff, J.D. Scott, The protein kinase A anchoring protein mA KAP coordinates two integrated cAMP effector pathways, *Nature*. 437 (2005) 574–578.
- [50] W. Schulze, I.B. Buchwalow, Adenylyl cyclase in the heart: an enzymocytochemical and immunocytochemical approach, *Microsc. Res. Tech.* 40 (1998) 473–478.
- [51] V. Timofeyev, R.E. Myers, H.J. Kim, R.L. Woltz, P. Sirish, J.P. Heiserman, N. Li, A. Singapur, T. Tang, V. Yarov-Yarovoy, E.N. Yamoah, H.K. Hammond, N. Chiamvimonvat, Adenylyl cyclase subtype-specific compartmentalization: differential regulation of L-type Ca^{2+} current in ventricular myocytes, *Circ. Res.* 112 (2013) 1567–1576.
- [52] R.A. Johnson, L. Desaubry, G. Bianchi, I. Shoshani, E. Lyons Jr., R. Taussig, P. A. Watson, J.J. Cali, J. Krupinski, J.P. Pieroni, R. Iyengar, Isozyme-dependent sensitivity of adenylyl cyclases to P-site-mediated inhibition by adenine nucleosides and nucleoside 3'-polyphosphates, *J. Biol. Chem.* 272 (1997) 8962–8966.
- [53] K. Iwatsubo, S. Minamisawa, T. Tsunematsu, M. Nakagome, Y. Toya, J. E. Tomlinson, S. Umemura, R.M. Scarborough, D.E. Levy, Y. Ishikawa, Direct inhibition of type 5 adenylyl cyclase prevents myocardial apoptosis without functional deterioration, *J. Biol. Chem.* 279 (2004) 40938–40945.
- [54] C.S. Brand, H.J. Hocker, A.A. Gorfe, C.N. Cavasotto, C.W. Dessauer, Isoform selectivity of adenylyl cyclase inhibitors: characterization of known and novel compounds, *J. Pharmacol. Exp. Ther.* 347 (2013) 265–275.
- [55] J.H. Braeunig, F. Schweda, P.L. Han, R. Seifert, Similarly potent inhibition of adenylyl cyclase by P-site inhibitors in hearts from wild type and AC5 knockout mice, *PLoS One* 8 (2013), e68009.
- [56] P. Mattick, J. Parrington, E. Odia, A. Simpson, T. Collins, D. Terrar, Ca^{2+} -stimulated adenylyl cyclase isoform AC1 is preferentially expressed in guinea-pig sino-atrial node cells and modulates the I_f pacemaker current, *J. Physiol.* 582 (2007) 1195–1203.
- [57] P.B. Nielsen, T.B. Larsen, A. Gorst-Rasmussen, F. Skjoth, G.Y. Lip, beta-blockers in atrial fibrillation patients with or without heart failure: association with mortality in a Nationwide cohort study, *Circ. Heart Fail.* 9 (2016), e002597.
- [58] A. Goette, J.M. Kalman, L. Aguinaga, J. Akar, J.A. Cabrera, S.A. Chen, S.S. Chugh, D. Corradi, A. D'Avila, D. Dobrev, G. Fenelon, M. Gonzalez, S.N. Hatem, R. Helm, G. Hindricks, S.Y. Ho, B. Hoit, J. Jalife, Y.H. Kim, G.Y. Lip, C.S. Ma, G.M. Marcus, K. Murray, A. Nogami, P. Sanders, W. Uribe, D.R. Van Wagoner, S. Nattel, EHRA/HRS/APHRS/SOLAECE expert consensus on atrial cardiomyopathies: definition, characterization, and clinical implication, *Heart Rhythm*. 14 (2017) e3–e40.
- [59] M.A. Walker, G.S.B. Williams, T. Kohl, S.E. Lehnart, M.S. Jafri, J.L. Greenstein, W. J. Lederer, R.L. Winslow, Superresolution modeling of calcium release in the heart, *Biophys. J.* 107 (2014) 3018–3029.